Building and Environment 285 (2025) 113596

Contents lists available at ScienceDirect

Building and Environment

journal homepage: www.elsevier.com/locate/buildenv

Advances and challenges in metal oxide semiconductor-based sensors for indoor ozone detection

Dongqing Pang [a,b], Enze Tian [c], Ruijie Xie [a,b,d], Ziquan Yin [a,b], Junquan Chen [a,b], Jiaojiao Deng [a,b,d,*], Jinhan Mo [a,b,d]

[a] *Key Laboratory of Coastal Urban Resilient Infrastructures (Ministry of Education), College of Civil and Transportation Engineering, Shenzhen University, Shenzhen 518060, China*
[b] *State Key Laboratory of Subtropical Building and Urban Science, Shenzhen University, Shenzhen 518060, China*
[c] *Songshan Lake Materials Laboratory, Dongguan 523808, China*
[d] *State Key Laboratory of Intelligent Geotechnics and Tunnelling, Shenzhen University, Shenzhen 518060, China*

ARTICLE INFO

Keywords:
Metal oxide semiconductor
Ozone sensor
Low-concentration detection
Structure-property correlation

ABSTRACT

Precise ozone (O_3) monitoring is critical for human health, building environment, medical sterilization, and industrial process control. Metal oxide semiconductor (MOS)-based sensors offer high sensitivity and easy miniaturization, making them attractive for O_3 detection, particularly in building and indoor air quality systems. Despite significant progress, a comprehensive analysis encompassing the fundamental sensing mechanism, material structure-property relationships, and performance enhancement strategies remains lacking. This review comprehensively elucidates the fundamental sensing mechanism of MOS-based O_3 sensors, including interfacial O_3 adsorption, charge transfer, and conductivity modulation. It also evaluates key performance metrics and the influence of environmental factors such as operating temperature, humidity, and lighting. Crucially, the correlations between material composition, microstructure, and sensing properties are analyzed to guide rational material design for robust performance in real-world applications like indoor monitoring. The development of gas sensor structures, from traditional sensors (sintered, thick film, and thin film types) to micro-electro-mechanical systems (MEMS) sensors and flexible sensors, was analyzed. Finally, emerging research directions aimed at improving sensitivity, lowering energy consumption, and enhancing operational stability for long-term indoor deployment are identified. These insights aim to support the development of next-generation MOS-based O_3 sensors for real-world applications.

1. Introduction

The acceleration of industrialization and urbanization has intensified global air pollution, making it a critical environmental and public health concern worldwide [1]. Among key atmospheric pollutants, tropospheric ozone (O_3), a secondary pollutant generated through photochemical interactions between volatile organic compounds (VOCs) [2,3] and nitrogen oxides (NO_x) [4], has emerged as a contributor to air quality degradation, particularly in industrial regions and in urban building environments where indoor ozone infiltration and indoor chemical reactions exacerbate exposure risks [5,6]. As a potent oxidant, O_3 contributes to respiratory dysfunction and chronic disease exacerbation [7], and is linked to an estimated 147,100 premature deaths globally in 2019 [8–10]. Indoor ozone exposure, originating from outdoor infiltration or indoor sources such as air purifiers and office equipment, further compounds these health risks, particularly in poorly ventilated residential and commercial spaces. Beyond its adverse human impacts, O_3 pollution undermines agricultural productivity [11,12], disrupts ecosystem integrity [13,14], and accelerates the degradation of materials, including infrastructure and cultural heritage [15–17].

To mitigate these risks, many countries, including China, the United States, Italy, and Japan, have established regulatory thresholds for ambient O_3 levels [10]. In 2021, the World Health Organization (WHO) revised its Air Quality Guidelines (AQGs), recommending a maximum daily 8-hour mean O_3 concentration of 100 $\mu g/m^3$ (50.11 ppb) for short-term exposure, and a seasonal 8-hour average not exceeding 60

---

* Corresponding author at: Key Laboratory of Coastal Urban Resilient Infrastructures (Ministry of Education), College of Civil and Transportation Engineering, Shenzhen University, Shenzhen 518060, China.

E-mail address: deng.jiaojiao@szu.edu.cn (J. Deng).

https://doi.org/10.1016/j.buildenv.2025.113596
Received 15 July 2025; Received in revised form 12 August 2025; Accepted 25 August 2025

μg/m^3 (30.07 ppb) over six consecutive months. Despite regulatory efforts, O_3 pollution remains a significant barrier to sustained improvements in air quality [18–20]. Consequently, precise and reliable O_3 monitoring has become indispensable across environmental science [21], industrial safety [22], and public health applications [23,24].

Meanwhile, O_3, with its strong oxidizing property, has been extensively utilized across various fields, such as industry, medicine, and agriculture. In industrial settings, O_3 at controlled concentrations facilitates the degradation of organic pollutants, the synthesis of photoresist, and the purification of water and air [25]. In medicine, the therapeutic applications of O_3 include the treatment of chronic wounds, peripheral arterial disease, intervertebral disc herniation, and various dental conditions, with integrated sensors enabling precise monitoring of exposure levels [26]. In medical applications, integrated sensors can precisely monitor ozone exposure levels and are commonly used in scenarios requiring ozone treatment, such as chronic wounds, peripheral artery disease, disc herniation, and a range of dental disorders [27].

O_3 sensors play a central role in applications ranging from human health, building environment, medical and sterilization applications, to industrial process control and safety. Depending on the sensing mechanisms, O_3 sensors can be broadly categorized into electrochemical [28, 29], optical [30,31], photoacoustic spectroscopic [32], and semiconductor-based devices [33]. As summarized in Table 1, each type of sensor offers analysis in terms of sensitivity, power consumption, cost, and operational lifespan. Electrochemical sensors offer high sensitivity but are frequently limited by short operational lifespans [34]. Optical sensors, characterized by exceptional precision and selectivity, are well-suited for specific high-accuracy applications. However, their complex structure and high production cost hinder widespread deployment [35]. Among these, metal oxide semiconductor (MOS)--based O_3 sensors present an alternative due to their low cost, ease of miniaturization, broad material compatibility, and compatibility with integrated electronic systems. Therefore, they have garnered significant research interest and are increasingly regarded as a promising platform for O_3 detection [36,37]. Despite their potential, MOS-based O_3 sensors face persistent performance bottlenecks, including insufficient sensitivity at low concentrations, slow response/recovery kinetics, vulnerability to environmental interferences, and long-term stability [38]. Addressing these constraints to enhance the overall performance of MOS-based O_3 sensors represents a key research priority.

Despite the widespread use of MOS materials in gas sensing, a systematic review comprehensively analyzing sensing mechanisms, material structure design strategies, and performance enhancement approaches for MOS-based O_3 sensors is notably lacking. To fill this gap, this paper reviews recent progress in MOS-based gas sensors, providing the research community with an accessible overview of advanced technologies. First, we outlined the basic principles for MOS-based O_3 sensing, including the working mechanism and performance evaluation indicators. Subsequently, we analyzed the influencing factors affecting sensor performance from three aspects: operating temperature, ambient humidity, and light conditions. We then critically reviewed recent advances in gas-sensitive materials for MOS-based O_3 sensors, encompassing material preparation, composition, and structure. An analysis was conducted on the structure of MOS-based O_3 sensing devices. Finally, we discussed the future directions, focused on innovations in composite material design, device manufacturing technology, multifunctional integration, and intelligent systems to enhance sensor performance and enable real applications. By integrating interdisciplinary insights from materials science, environmental engineering, sensor physics, and data science, this review can guide the development of portable, real-time O_3 monitoring devices suitable for various fields such as the environment, industry, and biomedicine.

2. MOS-based O_3 sensors

2.1. Sensing mechanism of MOS-based O_3 sensors

The working process of MOS-based O_3 sensors consists of two stages.

Stage 1: oxygen molecules in the ambient air are adsorbed on the sensor surface to form chemically adsorbed oxygen by capturing the electrons in the MOS material's conduction band (Eq. (1)), thereby establishing a stable baseline resistance [46,47], which is the "initialization" stage of the sensor. The type of chemically adsorbed oxygen is related to the operating temperature [48]. When the operating temperature is below 150 °C, the main form of chemically adsorbed oxygen is O_2^- (Eq. (2)). When the operating temperature is above 150 °C, oxygen mainly undergoes chemical adsorption, and the chemically adsorbed oxygen exists in the form of O^- (Eq. (3)). When the operating temperature exceeds 300 °C, the chemically adsorbed oxygen mainly exists in the form of O^{2-} (Eq. (4)). Meanwhile, the presence of chemically adsorbed oxygen increases the activity on the surface of MOS materials, which can further enhance their reaction with O_3 molecules.

$$O_2(gas) \rightarrow O_2(ads) \tag{1}$$

$$O_2(ads) + e^- \rightarrow O_2{}^-(ads) T < 150^\circ C \tag{2}$$

$$O_2{}^-(ads) + e^- \rightarrow 2O^-(ads) 150^\circ C < T < 300^\circ C \tag{3}$$

$$O^-(ads) + e^- \rightarrow O^{2-}(ads) T > 300^\circ C \tag{4}$$

Table 1
Summary of conventional O_3 sensing technologies.

Sensor type	Working principle	Advantages	Disadvantages	References
Electrochemical gas sensor	Electrochemical reaction	• High sensitivity; • Low power consumption; • linear response;	• Limited life; • Vulnerable to environmental interference;	[28,39, 40]
Optical gas sensor	Optical properties such as light absorption and emission by gas	• Low power consumption; • High stability; • High precision;	• Expensive; • Long response time; • Large volume;	[41–43]
Photoacoustic spectral gas sensor	Photoacoustic effects and the principles of optical spectroscopy	• High sensitivity; • Good selectivity; • Fast response speed;	• Expensive; • Large; • High environmental requirements;	[44]
MOS-based gas sensor	Oxidation-reduction reaction	• Low cost; • High sensitivity; • Easy to integrate; • Fast response speed;	• High power consumption; • Vulnerable to environmental influence; • Lack of stability	[45]

where, (gas) means the gas phase, referring to the existence of oxygen in gaseous form, and (ads) means the adsorbed content, referring to the state where oxygen is adsorbed.

> **Stage 2:** When there is O_3 in the air, as a strong oxidizing gas with high electron affinity, it will extract electrons from the conduction band or surface oxygen atoms of MOS materials, thereby reducing the carrier concentration. Specifically, O_3 will undergo redox reactions with surface active sites (Eq. (5)), inducing electron transfer on the MOS material surface and further altering the resistance [49]. Under certain operating temperatures or the excitation of active sites, the adsorbed O_3 will undergo oxidation–reduction reactions with metal atoms [50], oxygen vacancies [51,52], adsorbed oxygen [53] and other active sites on the surface (Eq. (6)), which leads to changes in the electronic structure of the material surface and causes alterations in the resistance of MOS materials.

$$O_3(gas) + e^- \rightarrow O_3{}^-(ads) \tag{5}$$

$$O_3{}^-(ads) + O^-(ads) + 2e^- \rightarrow O_2(gas) + 2O_2{}^-(ads) \tag{6}$$

The response to O_3 concentration can be achieved by comparing the resistance changes before and after O_3 exposure [45]. The variation law of the resistance of MOS-based O_3 sensors is closely related to the type of MOS materials. According to the difference of carriers, MOS materials can be roughly divided into n-type and p-type semiconductors [54,55]. In n-type materials, electrons are the main carriers, while in p-type materials, holes are dominant [56]. The working mechanism of the two types of MOS-based O_3 sensors is summarized in Fig. 1.

In n-type MOS materials, adsorbed oxygen molecules capture electrons from the conduction band, forming negatively charged oxygen species and inducing a positively charged electron depletion layer (EDL) at the surface. This process increases the surface potential barrier and raises the material's resistance. In contrast, in p-type MOS materials, oxygen adsorption leads to the withdrawal of electrons from the valence band, effectively increasing the surface hole concentration. This results in the formation of a hole accumulation layer (HAL), which lowers the potential barrier and decreases the resistance [58].

When O_3 gas interacts with the surface of n-type MOS materials, its strong oxidizing nature allows it to capture electrons from the conduction band. This process leads to a decreased concentration of surface electrons and a widening EDL [59]. Consequently, the potential barriers at grain boundaries are further heightened, impeding charge carrier transport, reducing electrical conductivity, and ultimately increasing the resistance of the sensing material. When p-type semiconductor sensors are exposed to O_3, the gas captures electrons from the semiconductor, increasing the hole concentration. The increase in hole density reduces both the thickness of the depletion layer and the surface potential barrier. The reduced barrier enhances carrier transport and conductivity, leading to a decrease in sensor resistance.

2.2. Evaluation index of O_3 sensing performance

The performance of an O_3 sensor can be reflected by multiple parameters, including response, response and recovery time, selectivity, and stability [60]. A comprehensive understanding of these parameters and their interactions is essential for designing advanced gas sensors.

(1) Response

Response is a critical performance metric in evaluating gas sensors. This metric reflects how the sensor's output varies with changes in gas concentration [61]. There are various methods for calculating response, as shown in Eqs. (7) and (8). Among them, Eq. (7) applies to scenarios that require high-sensitivity detection, while Eq. (8) is more suitable for high-concentration O_3 detection or stability testing.

$$S = (R_g - R_a)/R_a \tag{7}$$

$$S = R_g/R_a \tag{8}$$

where, S is the response, R_g is the resistance value exposed to the O_3 gas, and R_a is the resistance value when exposed to clean air.

The sensor's sensitivity refers to the change in response per unit of O_3 concentration, as shown in Eq. (9).

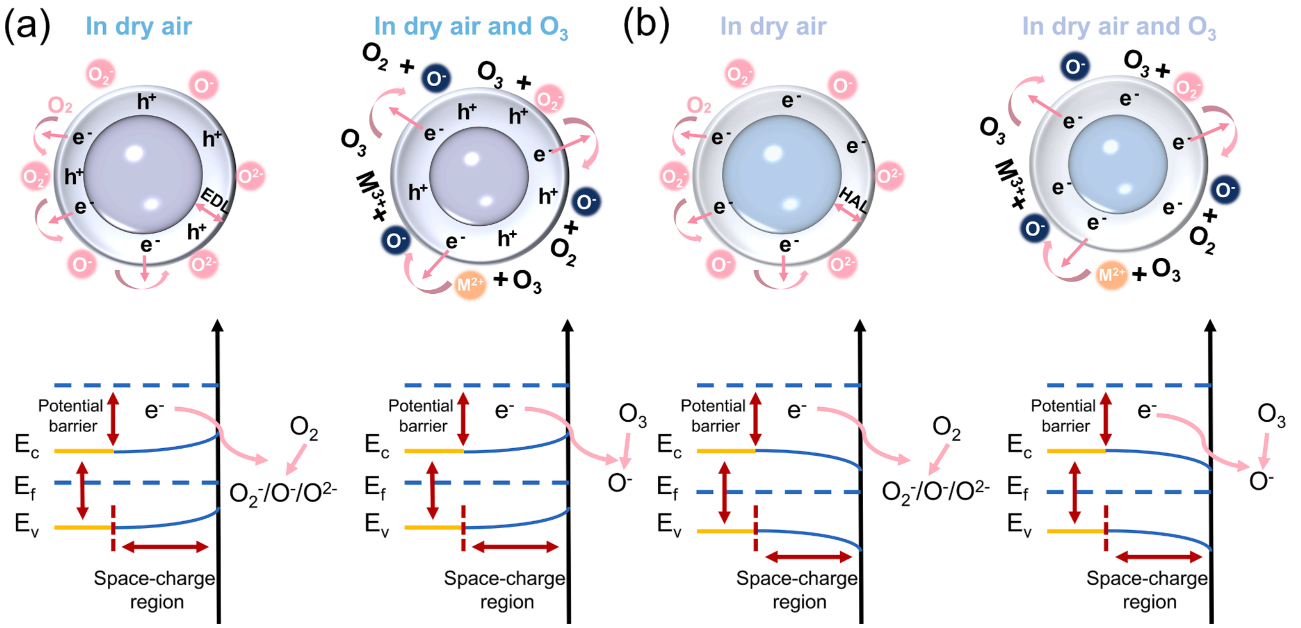

Fig. 1. Schematic illustration of the surface reaction mechanisms and energy band diagrams of (a) p-type and (b) n-type MOS materials in dry air and the presence of O_3. Reproduced with permission from Ref. [57], Copyright 2024 Elsevier.

$$Sensitivity = \frac{S}{C} \tag{9}$$

where, C is the O_3 concentration in the air.

(2) Response time

Response time t_{res} is the duration required for the sensor resistance to reach 90% of its total change upon exposure to the target gas. A shorter response time indicates a faster sensor reaction to dynamic gas concentration changes. This characteristic is critical for applications requiring real-time monitoring, such as industrial gas leak detection systems.

(3) Recovery time

Recovery time t_{rec} is the time required for the sensor resistance value to return to 10% of the baseline value after the target gas is removed. A rapid recovery time signifies the sensor's ability to swiftly reset to its initial state, enabling continuous monitoring in dynamic environments.

(4) Detection limit

The detection limit defines the concentration range that a gas sensor can reliably measure, from the low limit of detection (LOD) to the saturation concentration range. A lower LOD generally indicates higher sensor sensitivity and wider applicability.

(5) Stability

Stability reflects a gas sensor's ability to maintain consistent output signals over prolonged operation. It is generally classified into two components: active stability and conservative stability [62]. Active stability refers to the reproducibility of the sensor's response when repeatedly exposed to the same target gas at different times. Conservative stability pertains to the sensor's ability to retain its selectivity and sensitivity during sustained environmental exposure, ensuring consistent target gas discrimination and signal reliability over time.

Common methods for improving the stability of MOS-based sensors can be categorized into three main aspects: optimization of sensitive materials, regulation of the test environment, and design of the device structure [63]. In terms of sensitive materials, techniques such as thermal treatment can be utilized as a pre-treatment method. This process cleans the material's surface, removes impurities, and importantly, limits subsequent grain growth during operation [64]. For test environment regulation, temperature switches or modulation techniques can be employed to enhance sensor stability [65]. Concerning device structure design, optimizing factors such as microstructure and the type of film (thick or thin) can also contribute to improved stability [66].

(6) Selectivity

Selectivity denotes a gas sensor's ability to discriminate a target gas from interfering species [67]. This capability is crucial for accurate detection in complex environments, including environmental monitoring and biomedical diagnostics [68,69].

The primary strategies for enhancing selectivity in MOS-based sensors include designing advanced materials, optimizing operating temperature, and integrating gas filtration media. Advanced materials design focuses on tailored surface interactions through: (i) Catalyst-enabled surface modification/functionalization (using oxidizing/dissociation/adsorption catalysts), (ii) Defect engineering and structure control to modulate active sites, and (iii) Composite materials (e.g., conductive polymers) or chemical modifications (e.g., self-assembled monolayers) for molecular recognition and surface tuning [70,71]. Optimizing operating temperatures takes advantage of different gas response patterns that occur at specific temperatures. Techniques such as temperature switching or dynamic adjustments, combined with feature extraction, can enhance responsiveness to target gases [65]. Integrating gas filtration media helps to pre-screen interfering substances before detection. Together, these approaches enhance target recognition through catalytic optimization, molecular-specific interactions, and regulation of surface energy levels.

To fulfill the stringent requirements of diverse application domains, an ideal O_3 sensor should integrate exceptional selectivity with high sensitivity, rapid response and recovery, long-term stability, low detection limits, reduced power consumption, and facile integration into electronic platforms.

3. Influencing factors of MOS-based O_3 sensor performances

The performances of MOS-based O_3 sensors are critically determined by a complex interplay of external and intrinsic factors that include material surface reactions [72]. Among these, operating temperature, ambient humidity, and light conditions represent three critical parameters that significantly affect the performance of the MOS-based O_3 sensor.

3.1. Operating temperature

Operating temperature significantly affects the performance of MOS-based O_3 sensors by modulating surface reaction kinetics, carrier mobility [73], and adsorption-desorption dynamics [74], also intimately linked to power consumption [75,76]. Elevated operating temperatures enhance redox interactions and charge transfer efficiency, reducing resistance and improving sensitivity [15]. However, this thermal effect is inherently bidirectional. Excessive heat can disrupt the adsorption-desorption equilibrium, increase carrier scattering, and generate lattice defects, ultimately degrading sensitivity and stability [77]. Therefore, an optimal operating temperature exists where sensor performance is optimized by balancing reaction kinetics and material stability (Fig. 2a) [36]. Liu et al. [78] exemplify this duality through a systematic study of Co_3O_4-based O_3 sensors, demonstrating distinct resistance variations and selective responses to O_3 under different thermal conditions (Fig. 2b, c). Moreover, prolonged exposure to high temperatures may induce thermal expansion and irreversible microstructural changes, compromising sensing accuracy and long-term reproducibility [79,80]. These findings underscore the necessity of material-specific operating temperature optimization, as illustrated by In_2O_3/ZnO composites with varying In: Zn ratios in Fig. 2d, whose response to 1 ppm O_3 reveals dependence on both composition and thermal conditions [81].

3.2. Ambient humidity

Environmental humidity significantly affects the performance of MOS gas sensors by regulating surface chemical processes [82]. Water molecules adhere to the sensor surface through physical and chemical adsorption, altering the baseline resistance, sensitivity, and long-term stability. Physical adsorption mainly changes the dielectric environment and the depletion layer thickness, increasing carrier scattering. Chemical adsorption induces water molecules' dissociation into hydroxide ions (OH^-) and hydrogen ions (H^+) (Eq. (10)), which react with the adsorbed oxygen or compete for adsorption sites, thereby influencing gas response [83,84]. The effect of humidity is dual, either enhancing or suppressing the sensor's response. Therefore, it is necessary to perform material-specific optimization and environmental calibration.

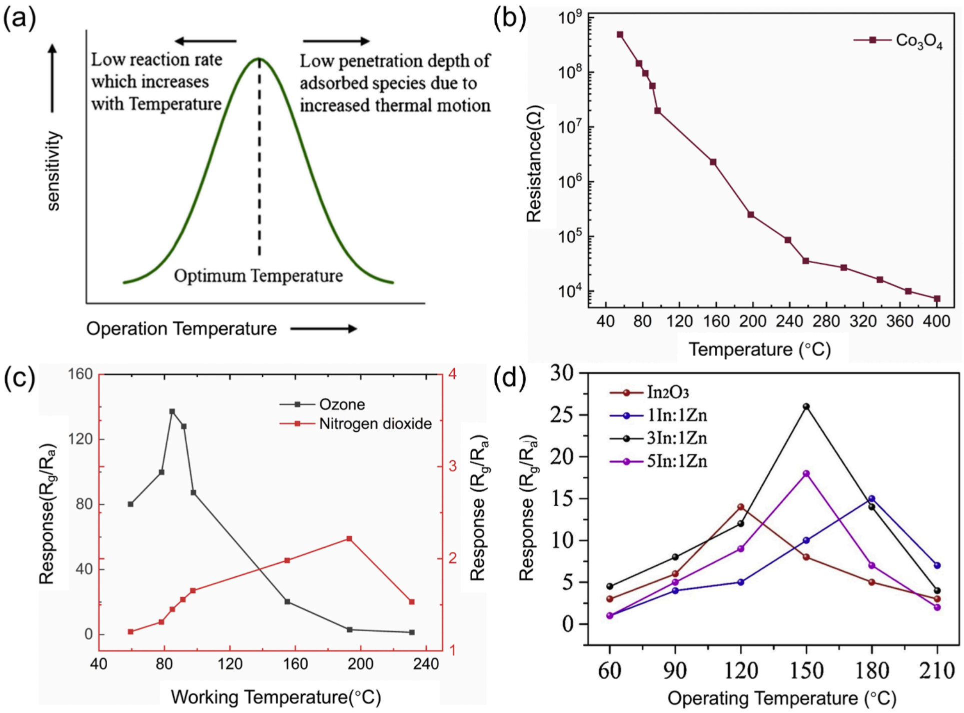

Fig. 2. (a) The resistance variation with temperature. There is an optimal value for the operating temperature. Reproduced with permission from Ref. [36], Copyright 2022 Springer Nature Link. (b) The resistance of the Co_3O_4 sensor varies with operating temperature. The resistance of the Co_3O_4 sensor decreases as the operating temperature increases, and the slope decreases when the operating temperature is over 260 °C. (c) The response variation to O_3 and NO_2 with operating temperature. The Co_3O_4 sensor shows selective gas-sensing to O_3 at low operating temperatures. Reproduced with permission from Ref. [78], Copyright 2019 Elsevier. (d) The responses of In_2O_3/ZnO composite with different molar ratios to 1 ppm O_3 gas at 60–210 °C. The response of all sensors shows the trend of "increasing-maximum-decreasing" to O_3. Reproduced with permission from Ref. [81], Copyright 2019 Elsevier.

(1) Positive effect of humidity

Water vapor can enhance MOS-based O_3 sensing through synergistic mechanisms. For one thing, upon adsorption, water molecules dissociate on the sensor surface, injecting electrons into the sensing layer. These electrons recombine with holes, diminishing the HAL and amplifying the response. For another, the dissociation products (hydroxyl groups and hydrogen atoms) act as reactive intermediates that facilitate O_3 decomposition (Eqs. (11)–(13)), further enhancing the response. Experimental studies confirm this enhancement. Zhu et al. [85] reported increased O_3 sensitivity in Ag-In_2O_3 composites with rising humidity. Fig. 3a illustrates the moisture-modulated reaction pathway. Lai et al. [86] observed similar behavior in CuO nanowires: response to 200 ppb O_3 increased from 6.7% (50% RH) to 17.8% (90% RH), as shown in Fig. 3b.

$$H_2O \rightarrow H^+ + OH^- \tag{10}$$

$$O_3(gas) + H^+ + 2e^- \rightarrow O_2(gas) + OH^- \tag{11}$$

$$O_3(gas) + 2OH^- \rightarrow O_2(gas) + 2O^-(ads) + H_2O \tag{12}$$

$$2O^-(ads) \rightarrow O_2(gas) + 2e^- \tag{13}$$

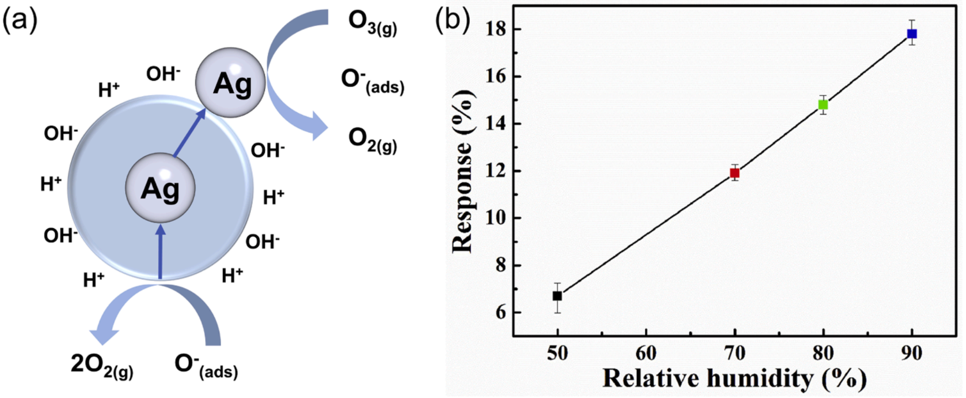

Fig. 3. (a) Scheme of the O_3 reaction mechanism for the Ag-In_2O_3 sensing material. Water molecules are adsorbed at the adsorption sites on the surface of Ag-In_2O_3, resulting in the dissociation of water molecules into hydrogen ions and hydroxyl groups. O_3 gas molecules interact directly with hydrogen ions and hydroxyl groups, and the presence of Ag further enhances the reaction rate. Therefore, the Ag-In_2O_3 response increases with increasing humidity. Reproduced with permission from Ref. [85], Copyright 2016 Elsevier. (b) The sensor's response of 3.3 μm CuO NWs gas sensor to 200 ppb O_3 at 25 °C with relative humidity ranging from 50% to 90%, the response increased with increasing humidity. Reproduced with permission from Ref. [86], Copyright 2024 Elsevier.

(2) Negative effects of humidity

Ambient humidity also critically degrades the sensitivity and reliability of MOS-based gas sensors [87]. Hydroxyl groups from water dissociation occupy surface active sites, inducing competitive adsorption with O_3 and limiting the interaction between O_3 and the sensing material [88]. This competitive adsorption effect is particularly pronounced in high-humidity conditions [89,90]. Zhu et al. [91] demonstrated this phenomenon using Au@TiO_2 core-shell nanoparticles. They found that water molecules preferentially adsorb at hydroxyl-rich TiO_2 surfaces under increasing relative humidity, forming a stable hydrogen-bond network that blocks the O_3-active site. Consequently, the sensor's response dropped from 4.36 at 30% RH to 2.32 at 70% RH.

3.3. Lighting condition

A light source with a specific wavelength can provide sufficient photon energy to excite the valence band electrons in MOS materials, allowing them to transition to the conduction band. This process generates electron-hole pairs, which can influence the rates of gas adsorption-desorption, ultimately enhancing the O_3 response of the sensor pair (Fig. 4a) [92,93]. Ultraviolet light (UV) is widely used as a light source because its photon energy is higher than the band gap of most MOS materials. Wu et al. [94] confirmed that UV-LED at 365 nm could detect O_3 levels lower than 5 ppb in an Indium-Gallium-Zinc Oxide (IGZO) film. And with the increase in light intensity, the selectivity significantly improves by more than 60% (Fig. 4b). Furthermore, in MOS materials with heterogeneous structures or specific defect engineering, the electron-hole pairs generated by photoexcitation can be effectively separated (Fig. 4c), thereby enhancing the charge collection efficiency. Huang et al. [95] developed a self-powered sensor composed of Cu_2O-coated Si nanowires (SiNWs). They found that visible light-enhanced charge collection (Fig. 4d) enables the device to generate an open-circuit voltage of 0.36 V, with a response of 47% to 10 ppm O_3. It exhibits excellent selectivity and long-term stability (Fig. 4e). Meanwhile, the electron holes generated by photoexcitation increase the surface-active sites, enhancing the gas adsorption and improving sensitivity. Huang et al. [96] demonstrated that 350 nm UV enhanced reactive oxygen species generation in ZnSnO/graphene nanocomposites (ZTO/GNS), resulting in high response and long-term stability towards 5 ppm O_3 (Fig. 4f).

Overall, the operating temperature plays a critical role in regulating surface redox reactions and charge carrier kinetics, with an optimal value that must be precisely tuned to maximize sensor performance. Environmental humidity exhibits a dual behavior. Moderate humidity levels can promote O_3 decomposition and regulate carrier migration through hydroxyl-mediated reactions, whereas excessive humidity hinders sensitivity through competitive adsorption and site blocking. Furthermore, photo-assisted activation, especially under ultraviolet

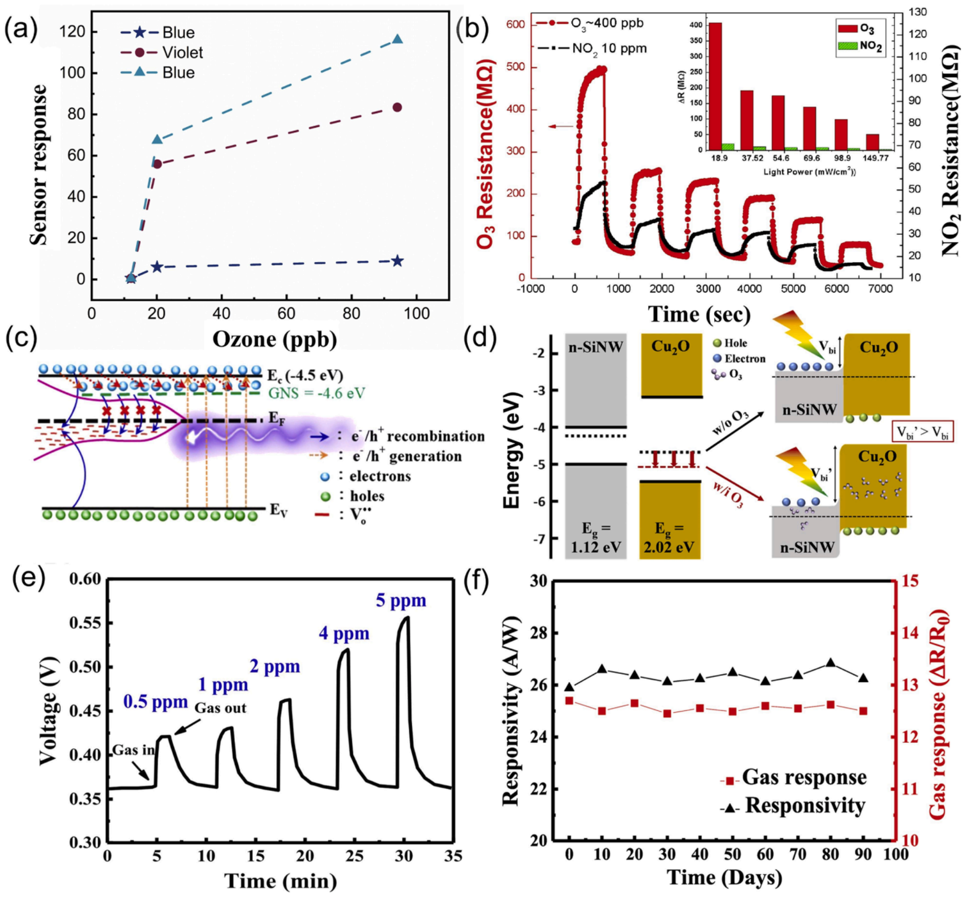

Fig. 4. (a) Light-assisted O_3 sensing response of a nanocrystalline SnO_2 sample as a function of O_3 level. Reproduced with permission from Ref. [93], Copyright 2022 Elsevier. (b) The resistance-time curves of O_3 and nitrogen dioxide under different light intensities. Reproduced with permission from Ref. [94], Copyright 2018 Elsevier. (c) Energy band diagram under UV illumination of ZTO/GNS. Under UV irradiation, after adding GNS to the ZTO layer, the recombination of photo-generated electron/hole pairs is inhibited. Reproduced with permission from Ref. [96], Copyright 2022 Elsevier. (d) Schematic diagram of the energy band structure for the p-Cu_2O/n-SiNW heterojunction under light illumination in the absence/presence of O_3 gas molecules. The visible light enhanced charge collection. (e) The V-T curve of a self-powered p-Cu_2O/n-SiNW gas sensor exposed to O_3 concentrations from 500 ppb to 5 ppm. Reproduced with permission from Ref. [95], Copyright 2022 Elsevier. (f) Responsivity and gas response as a function of storage time. Reproduced with permission from Ref. [96], Copyright 2022 Elsevier.

irradiation, can achieve efficient electron-hole generation and separation. This process increases surface active sites and enables low-power operation at room temperature (RT).

4. MOS material design for O_3 sensors

The performances of O_3-sensitive MOS sensors, such as sensitivity, selectivity, and long-term stability, can be optimized through rational material design with tailored material components and high-surface-area nanostructures. This chapter summarizes major synthesis strategies of MOS sensing materials and then reviews recent progress on engineering material components and nanostructures for advanced O_3 sensors.

4.1. Synthesis strategies of MOS sensing materials

The synthesis strategy of MOS materials is crucial for adjusting parameters such as the microstructure, crystallinity, and surface chemical properties of the materials, which directly affect the gas-solid interaction and sensing performance. To adjust the inherent properties of sensing materials, various synthesis techniques have been adopted, including solvothermal method [97], solution combustion and chemical precipitation method [98], lithography or laser ablation [99], spray pyrolysis [100], ion layer adsorption and reaction (ILGAR) [101], plasma-enhanced chemical vapor deposition (PECVD) [102], atomic layer deposition (ALD) [101]. Among them, solvothermal synthesis is the most commonly used method for preparing powder materials. Gas-sensitive films can then be fabricated through screen printing or drop coating [103]. RFMS and ALD are commonly used methods for directly fabricating gas-sensitive films, which will be discussed in detail as follows.

4.1.1. Solvothermal synthesis

Solvothermal synthesis enables precise control over the nucleation and growth of MOS material by adjusting precursor concentration, temperature, and reaction time [104]. Therefore, material morphology, crystal phase, and surface chemistry can be regulated towards boosted gas-sensing properties. As a typical example, Sui et al. [105] prepared In_2O_3 nanomaterials through sequential stages: raw material mixing, nucleation growth, self-assembly, and final high-temperature calcination for removing the organic templates (Fig. 5a). The precursor ratio, bath temperature, and solvothermal reaction time were adjusted to tailor the crystal phases of In_2O_3 nanomaterials. The resulting cubic bixbyite-type (C-In_2O_3), rhombohedral corundum-type (Rh-In_2O_3) and mixed phase In_2O_3 (Rh+*C*-In_2O_3) exhibited distinct chemisorbed oxygen (O_c) content (31.8%, 8.9% and 28.3%, respectively) (Fig. 5b) and band gap widths (2.38, 2.73 and 2.51 eV, respectively) (Fig. 5c). The narrow band gap is conducive to promoting electron excitation, increasing the carrier mobility rate, and at the same time, the high content of O_c can provide more active sites, enhancing the adsorption performance for O_3. Therefore, C-In_2O_3, with the narrowest band gap and highest O_c, delivered the strongest response (11.7 to 100 ppb O_3), while Rh-In_2O_3 showed significantly lower sensitivity (5.7) (Fig. 5d). Further advancement was reported by Zhang et al. [81], further enhancing O_3 sensing by constructing In_2O_3/ZnO hollow microtube composites through a dual-step solvothermal process (Fig. 5e). The introduction of Zn^{2+} increased surface oxygen vacancies and enabled the formation of an n-n heterojunction, collectively boosting charge separation and oxygen

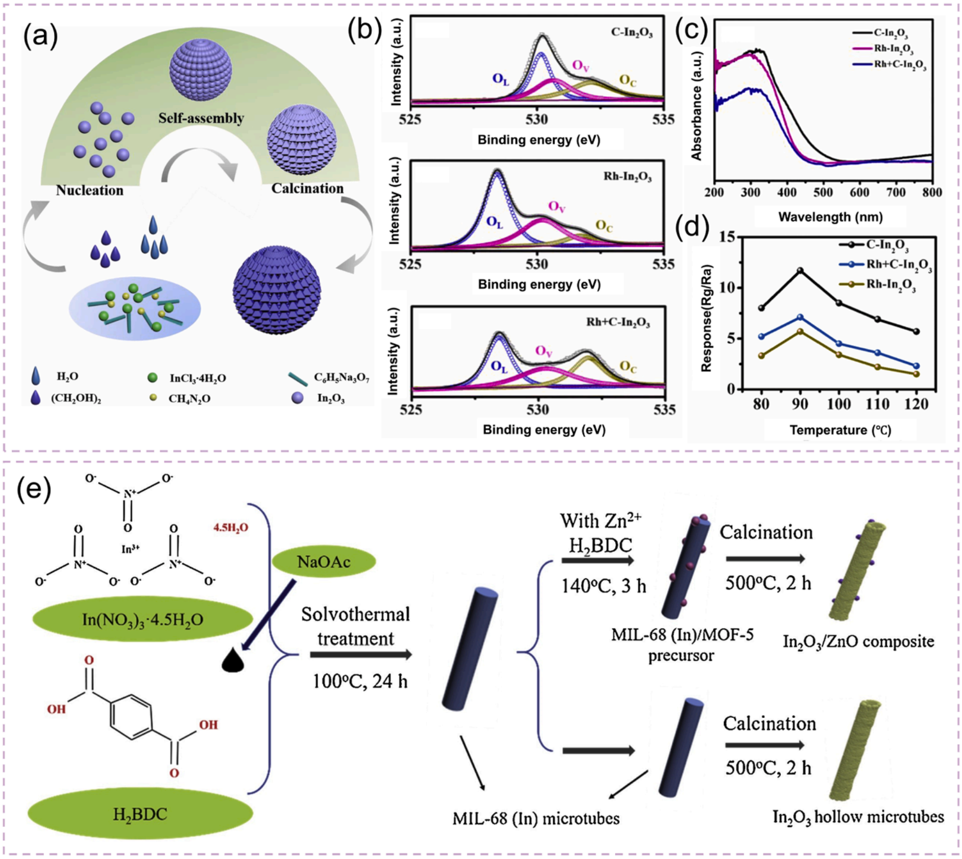

Fig. 5. (a) The formation mechanism of the In_2O_3 nanostructures. (b) XPS patterns for O 1 s of C-In_2O_3, Rh-In_2O_3 and Rh+*C*-In_2O_3. (c) The UV–visible absorption spectra of C-In_2O_3, Rh+*C*-In_2O_3 and Rh-In_2O_3. (d)The responses of three materials to 100 ppb O_3 at different operating temperatures. Reproduced with permission from Ref. [105], Copyright 2021 Elsevier. (e) Schematic illustration for preparing In_2O_3 hollow microtubes and In_2O_3/ZnO composite. Reproduced with permission from Ref. [81], Copyright 2019 Elsevier.

adsorption.

4.1.2. Radio-frequency magnetron sputtering

RFMS is a versatile physical vapor deposition technique that utilizes orthogonal electric and magnetic fields to generate argon plasma. The as-produced plasma ions bombard a target material to release atomic species that uniformly deposit onto substrates, forming a dense and uniform film. De Lima et al. [106] utilized RFMS to deposit ZnO nanoparticles on the rGO surface to produce rGO-ZnO nanocomposites. Fine-tuned interfacial properties were achieved through exacting nanoparticle size and morphology control, which are critical for boosting gas sensing performances (Fig. 6a). Xu et al. [107] developed an advanced approach combining glancing angle deposition (GLAD) with a reactive gas pulsing protocol (RGPP) during direct-current reactive magnetron sputtering. Tungsten oxide films with tailored sawtooth morphologies were produced (Fig. 6b), which significantly enhance gas diffusion and adsorption kinetics.

4.1.3. Atomic layer deposition

ALD is a vapor-phase thin film growth technique characterized by atomic-scale precision and exceptional conformality. It relies on sequential, self-limiting surface reactions between alternating gaseous precursors and the substrate. Each cycle deposits a single atomic or molecular layer, followed by inert gas purging to remove residual species. By controlling deposition cycles, the film thickness can be finely tuned with sub-nanometer accuracy, which is ideal for uniform and conformal coatings on substrates with complex topographies. Wu et al. [108] utilized ALD to deposit highly uniform ZnO films at 150 °C, achieving precise coverage and consistency of sensing properties across large-area substrates (15.6×15.6 cm^2, Fig. 7). In addition to the meticulous thickness control, the ALD growth also ensures strong film adhesion and minimal defects, thereby enhancing O_3 sensors' long-term stability and reliability.

A comparative evaluation of MOS-based O_3-sensing materials fabricated via solvothermal synthesis, RFMS, and ALD is summarized in Table 2. RFMS yields uniform and adherent films that align well with microfabrication processes; however, defect-related degradation may compromise long-term stability. ALD offers atomic-level precision, resulting in highly uniform and conformal coatings that are particularly suited for long-life sensors. Nevertheless, this method can be costly and exhibits limitations in terms of scalability. The solvothermal synthesis approach presents several advantages, including the production of high-purity crystalline phases, the utilization of eco-friendly reaction media, and compatibility with a variety of dopant incorporation strategies. In summary, solvothermal methods are advantageous for scalable and cost-effective fabrication, ALD excels in precision and reliability, while RFMS provides a balanced approach for the miniaturization and integration of sensors.

4.2. Material components

O_3 sensing performances of MOS materials, such as O_3 adsorption efficiency and charge transfer kinetics, are primarily governed by their intrinsic physicochemical properties, particularly surface defect density and charge carrier dynamics [109]. These critical properties can be precisely engineered through material design strategies ranging from controlled synthesis of single-component oxides to elemental doping and heterostructure construction, each approach offering distinct pathways to enhance surface reactivity and electronic properties for optimized O_3 detection sensitivity.

4.2.1. Single-component MOS materials

The selection of MOS materials plays a decisive role in determining the performance of O_3 gas sensors, primarily through the regulation of microstructure and electronic properties [109]. The key microstructural features, such as grain size, specific surface area, and surface defect density, directly determine O_3 adsorption efficiency and surface reactivity. Meanwhile, the electronic structures, including band gap, carrier concentration, and surface state, govern the charge transfer process between the gas molecule and the sensing material and determine the gas detection sensitivity.

Table 3 provides a comparative summary of commonly studied single-component MOS materials for O_3 sensing. Materials such as In_2O_3 [110], ZnO [111], SnO_2 [112], and WO_3 [113] exhibit distinct sensing characteristics across varying O_3 concentrations and operating temperatures. For instance, In_2O_3 displays a wide response range (4–353.26) over 10–1200 ppb O_3, especially under UV activation at RT. ZnO demonstrates stable O_3 sensing performance even at elevated operating temperatures (200–300 °C), with responses up to 90.5 at 100 ppb. In contrast, SnO_2 and WO_3 generally display lower responses under similar conditions.

However, conventional single-component MOS often faces inherent limitations in O_3 sensing due to insufficient surface reactivity and poor gas adsorption [130]. To address these challenges, researchers have developed material engineering strategies focusing on both chemical composition modification [131] and microstructural optimization [132]. These approaches enhance surface catalytic reactivity and charge transfer efficiency, leading to significant improvements in sensitivity, selectivity, response speed, and long-term stability [60,130].

4.2.2. Multi-component materials

(1) Hetero-elemental doped MOS materials

Hetero-elemental doping has emerged as an effective strategy for enhancing MOS-based O_3 sensing performance by precisely engineering material properties through foreign atom incorporation. This approach

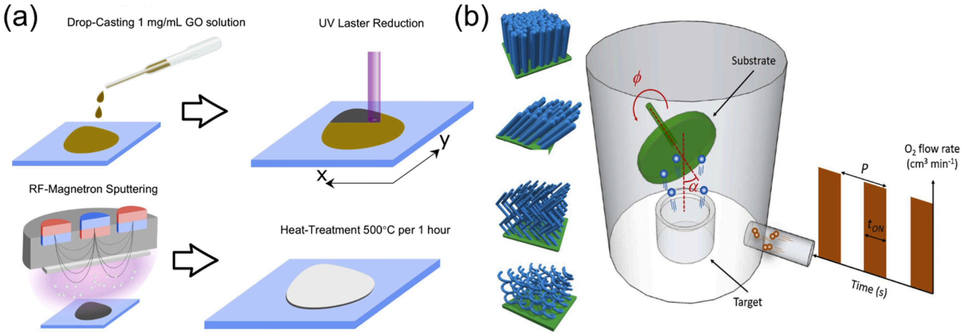

Fig. 6. Preparation process of radio frequency magnetron sputtering technology. (a) Schematic representation of the experimental setup for the rGO-ZnO nanocomposites preparation. Reproduced with permission from Ref. [106], Copyright 2021 Elsevier. (b) Schematic illustration of the GLAD and RGPP sputtering techniques used to prepare tungsten oxide thin films with normal, inclined, zigzag, and spiral columnar architectures. Reproduced with permission from Ref. [107], Copyright 2018 Elsevier.

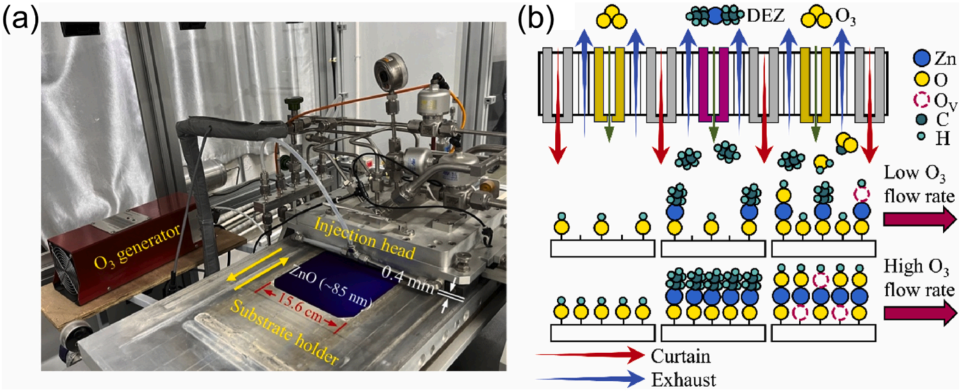

Fig. 7. Preparation process of atomic layer deposition technology. (a) SALD equipment photograph. (b) Deposition mechanism for the ZnO films prepared at low and high O_3 flow rates. Where O_v is oxygen vacancy. Reproduced with permission from Ref. [108], Copyright 2024 Elsevier.

Table 2
Comparative analysis of common preparation processes of MOS gas-sensitive materials.

Methods	Characteristics	Gas sensitivity	Key parameters	Limitation
Solvothermal synthesis`	• Nanostructure; • High specific surface area; • High crystallinity and few defects;	• High sensitivity; • Selective morphology and surface modification; • Porous structures for fast response speeds;	• Temperature; • Pressure; • Reaction time; • Precursor concentration;	• Poor repeatability; • Difficulty in mass production;
RFMS	• Dense and uniform film; • Adjustable film thickness; • Enhance crystallinity;	• Medium sensitivity; • Fast response speed; • Susceptibility to humidity;	• Power; • Air pressure; • Substrate temperature; • Sputtering time;	• Complex process parameters; • Difficult industrial production;
ALD	• Ultra-thin and uniform film; • Good controllability; • Avoid substrate damage;	• High sensitivity; • Adjustable selectivity by doping; • Slow response speed;	• Precursor pulse time; • Reaction temperature; • Cycle number;	• Slow sedimentation; • High cost;

Table 3
Performance comparison of commonly used single MOS gas-sensitive materials for O_3 sensing.

Material	Concentration/ ppb	Response (R_g/R_a)	Operating temperature/ °C	References
In_2O_3	10	4	RT+UV	[114]
	100	5.7	120	[105]
	100	16.7	80	[115]
	200	20	100	[116]
	200	5	70	[117]
	500	6.3	150	[118]
	1000	1000	250	[119]
	1000	14.08	150	[81]
ZnO	2500	1300	/	[120]
	280	100	200	[121]
	100	6.2	200	[99]
	60	3	250	[111]
	100	5.2	250	[111]
	100	90.5	300	[122]
	130	14	300	[123]
	130	14	300	[123]
	60	8	300	[124]
SnO_2	1000	1000	200	[112]
	58	1.1	20	[125]
	500	3	RT	[126]
WO_3	30	16	250	[127]
	500	3.9	150	[113]
$CuWO_4$	50	4.2	250	[128]
Mn_3O_4	5000	1.62	RT	[129]

enables controlled modulation of both electronic structures and surface characteristics, leading to improved sensitivity, selectivity, and response kinetics [133]. Hetero-elemental doping is typically classified into two categories based on the chemical nature of the dopants: metal doping and non-metal doping [134]. Metal dopants can reduce the bandgap and facilitate electron excitation into the conduction band, thereby accelerating the sensor's response to O_3 [135–137]. For example, incorporating highly conductive silver (Ag) into the In_2O_3 lattice significantly enhances electron transport properties [85]. Moreover, metal doping can alter the lattice spacing and coordination environment of atoms [138], promoting the formation of oxygen vacancies in the doped MOS materials [139–141]. As a typical example, Catto et al. [142] fabricated Co-doped ZnO thin film sensors, where Co^{2+} substitution for Zn^{2+} altered the local structure (Fig. 8a), increased oxygen vacancy concentration, and facilitated O_3 adsorption. The catalytic activity of cobalt also reduced the activation energy for the gas-solid reaction, significantly improving O_3 sensitivity at low operating temperatures (Fig. 8b). Similarly, Onofre et al. [100] synthesized $Zn_{0.95}Co_{0.05}O$ nanocrystalline thin films with high O_3 selectivity. Cobalt doping introduced both impurity states and structural defects, generating additional adsorption sites (Fig. 8c) and accelerating electron transport. These defect-induced active sites preferentially adsorb O_3, enabling detection limit as low as 20 ppb and markedly improving the O_3 selectivity (Fig. 8d).

Doping with non-metallic elements offers an effective approach to tailoring the electronic configuration and surface chemistry of MOS, thereby modulating their O_3^-sensing performance [143]. Notably, non-metal dopants with distinct electronegativity or bonding tendencies can alter the adsorption dynamics for target gas species because of varying electronic structures and porosity properties. For instance, Abbasi et al. [30] demonstrated that nitrogen doping in TiO_2/WSe_2 nanocomposites introduced hole carriers and modified the electronic structure, thereby enhancing O_3 molecule adsorption. Similarly, Korotcenkov et al. [144] found that selenium doping in In_2O_3 (Se-In_2O_3) can enhance O_3 permeability by creating micropores (10–400 nm) that enhance gas diffusion. Further supporting this, Moeini et al. [145] examined the O_3 adsorption behaviors on pristine BC_2NNTs and those doped with Al, Ga, Si, and Ge by using density functional theory (DFT)

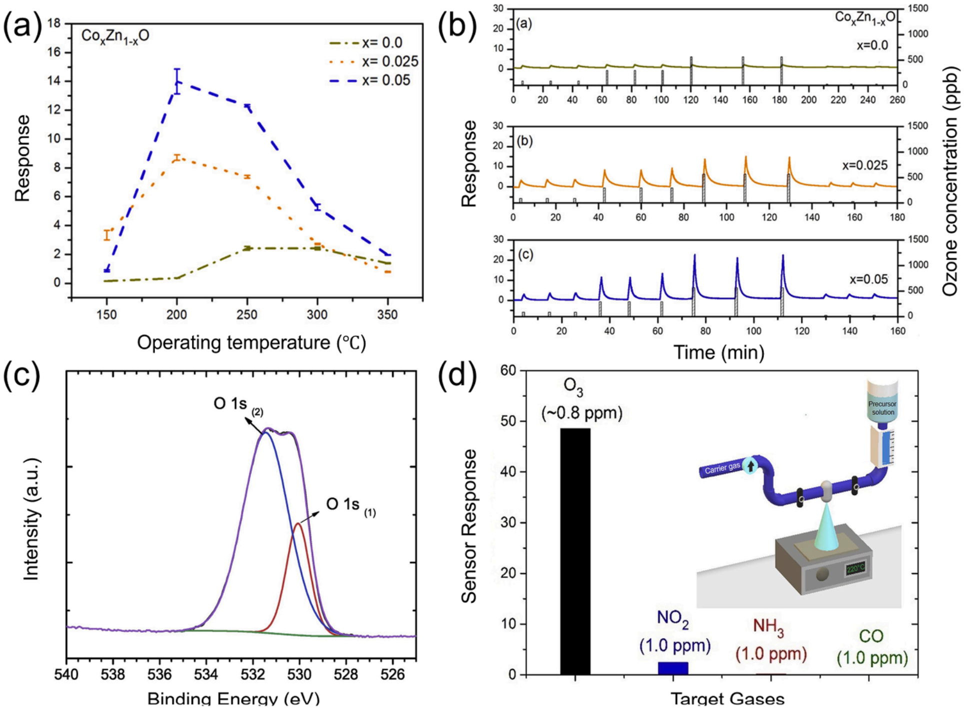

Fig. 8. (a) Gas sensor's response of the $Co_xZn_{1-x}O$ samples when exposed to 84 ppb of O_3 as a function of the operating temperature. The maximum response operating temperature decreased from 250 °C for $x = 0.0$ to 200 °C for $x = 0.05$, indicating that Co doping enhanced the ZnO sensor's response and provided additional sites for O_3 adsorption. (b) Gas-sensing response of the $Co_xZn_{1-x}O$ thin films exposed to different O_3 levels (42, 84, 290, and 560 ppb) at 200 °C. Reproduced with permission from Ref. [142], Copyright 2016 American Chemical Society. (c) XPS spectra of the as-prepared $Zn_{0.95}Co_{0.05}O$ sample of O 1 s. The O 1 s spectrum of the $Zn_{0.95}Co_{0.05}O$ sample, deconvoluted into O $1s_{(1)}$ (530.1 eV) and O $1s_{(2)}$ (531.2 eV), is attributed to the existence of oxygen vacancies or defects at the sample surface or oxygen-deficient regions within the ZnO lattice. The O $1s_{(1)}$ peak corresponds to the oxygen species located in a lattice bound to the metal cations (Zn^{2+} or substitutional Co^{2+}), while the O $1s_{(2)}$ peak reveals the presence of hydroxyl groups adsorbed on the sample surface. (d) Comparison of the sensor's responses of the $Zn_{0.95}Co_{0.05}O$ thin film exposed to different gases at an operating temperature of 250 °C. Reproduced with permission from Ref. [100], Copyright 2019 Elsevier.

simulations. Their findings revealed that the electron affinity difference between the dopant atoms and the gas-phase O_3 critically governs adsorption strength and charge transfer dynamics.

(2) Composite MOS materials

Constructing MOS composites is another attractive strategy to enhance the O_3 sensing performance. The incorporation of secondary materials can modulate surface chemistry, optimize charge transport pathways, introduce cooperative catalytic sites, and tune the electronic structure of the sensing matrix [30,146].

The combination of two or more materials with different band structures enables heterojunction formation, which regulates electron transport pathways [106,147], enhances charge separation efficiency, and improves gas molecule transport characteristics [148,149]. For instance, Sui et al. [150] fabricated n-n type In_2O_3/ZnO heterostructures where the interface induced an additional EDL, enhancing O_3 adsorption sites and improving interfacial charge separation (Fig. 9a). As a result, the composite demonstrated a linear response in the 15–260 ppb O_3 range, with an optimal operating temperature of 110 °C and rapid dynamics (235 s response time, 44 s recovery time at 15 ppb) (Fig. 9b). Similarly, Zhu et al. [151] developed p-n heterojunction nanocomposites by combining Cu_2O with rGO. The interfacial heterojunction promoted efficient photogenerated charge separation, suppressed electron-hole recombination, and enhanced selective interaction with O_3 molecules (Fig. 9c). Zhang et al. [81] derived In_2O_3 from MOF and ZnO nanoparticles to form an n-n heterojunction. Upon O_3 exposure, the interfacial depletion region between In_2O_3 and ZnO was widened due to decreased carrier concentration, leading to elevated sensor resistance and improved sensitivity (Fig. 9d, e). Under optimum operating temperature (150 °C), with In_2O_3 ($S = 14.08$, t_{res}/t_{rec} time of 43/77 s) compared to the In_2O_3/ZnO compound sensor for 1 ppm O_3 shows higher and faster response ($S = 26.12$, t_{res}/t_{rec} of 21/42 s).

Overall, O_3-sensing performances of MOS materials are fundamentally governed by their microstructures and electronic properties. Single-component MOS materials often exhibit limitations in sensitivity, response speed, and power consumption. Element doping proves particularly effective in regulating the carrier concentration and oxygen vacancy density, thereby enhancing the electronic properties and gas reactivity. Moreover, material hybridization and heterojunction engineering can enhance gas adsorption and charge transfer capabilities, ultimately leading to superior sensing responses. These approaches can collectively address the intrinsic limitations of MOS sensing materials while unlocking new possibilities for fabricating high-performance O_3 sensors.

4.3. Nanostructure design of O_3 sensing materials

Nano-structuring is a fundamental strategy for structurally optimizing gas-sensing materials. Reducing particle size to the nanoscale significantly increases the proportion of surface atoms, thereby enhancing the density of active adsorption sites for O_3 molecules [152,153]. Different nanostructures exhibit distinct porosity characteristics and surface topographies, which directly influence gas transport mechanisms [104,154,155]. These nanostructures are systematically classified by dimensionality as zero-dimensional (0D), one-dimensional (1D), two-dimensional (2D), and three-dimensional (3D) architectures [60], with each category exhibiting unique sensing-relevant characteristics.

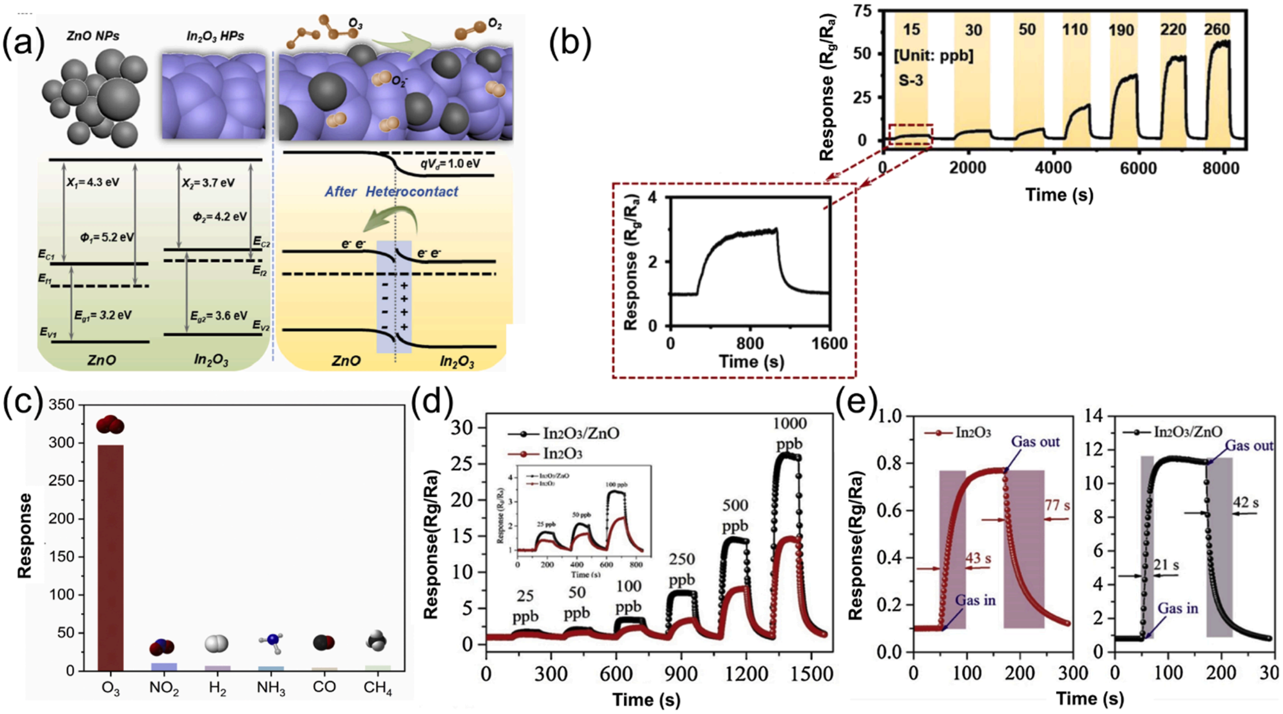

Fig. 9. (a) O_3 sensing mechanism and band variation of n-n heterojunction. For pure In_2O_3 HPs, the electron depletion layer only existed on the surface of sensing layers, whereas the uniform loading of n-type ZnO NPs to n-type In_2O_3 HPs could lead to a noteworthy n-n heterogenous interaction at the physical interface of composites, inducing an additional thickness modulation of the electron depletion layer. (b) Response transients of the sensor to 15–260 ppb of O_3. The lower left figure shows the transient response diagram of the sensor to 15 ppb O_3 after magnification. Reproduced with permission from Ref. [150], Copyright 2023 Elsevier. (c) Response curves of the In_2O_3 and 3In:1 Zn sensors toward different concentrations of O_3 gas at 120 °C and 150 °C. Reproduced with permission from Ref. [151], Copyright 2024 Elsevier. (d) Sensor's response of 0.5 wt% rGO—Cu_2O upon exposure to various gases at RT. (e) Response-recovery curves of In_2O_3 and 3In:1 Zn sensor toward 500 ppb O_3 gas. Reproduced with permission from Ref. [81], Copyright 2019 Elsevier.

4.3.1. 0D nanostructures

0D nanostructures, typically represented by nanoparticles and quantum dots (QDs), are often characterized by their near-point entities. These structures exhibit a high surface-to-volume ratio, elevated surface energy, and a substantial density of unsaturated surface atoms. Therefore, abundant active sites are provided for molecular adsorption and facilitate surface reactions, enabling highly sensitive detection of O_3 at trace concentrations [123]. 0D nanostructure design of MOS-based O_3 sensing materials has demonstrated significantly boosted sensitivity and selectivity. Catto et al. [128] synthesized $CuWO_4$ nanoparticles via an ultrasonic-assisted method (Fig. 10a) and found that higher annealing temperatures improved particle uniformity and size, and had a higher response to 90 ppb O_3 (Fig. 10b). In addition, Tseng et al. [156] employed a successive ionic layer adsorption and reaction technique to deposit Mn_3O_4 nanoparticles onto InGaZnO (a-IGZO) films (Fig. 10c), producing an increased oxygen vacancy density (Fig. 10d) and improved gas adsorption. And the as-fabricated MOS-based O_3 sensors demonstrate significant improvements in both sensitivity and selectivity (Fig. 10e).

QDs, as semiconductor nanocrystals typically smaller than 10 nm, exhibit unique photoelectric properties due to quantum confinement effects. Their ultrafine size, high specific surface area, and abundant active sites render them suitable for sensitive gas sensing at room temperature [157,158]. Kumar et al. [159] synthesized lead sulfide (PbS) quantum dots using a hot-injection technique, achieving nanocrystals with diameters of approximately 3–4 nm (Fig. 11a, b), markedly increasing the surface area available for O_3 adsorption and catalytic reaction. This nanoscale design significantly enhanced O_3 adsorption/catalytic surface and the intrinsic quantum confinement effect enabled efficient photoinduced charge generation/separation under fluorescent light. A photoactivated O_3 sensor was constructed as illustrated in Fig. 11c. An ultralow detection limit of 1.34 ppb for O_3 was achieved, outperforming commercial optical sensors. Moreover, the response/recovery time ratio to 500 ppb O_3 was determined to be as low as 1.18 (Fig. 11d).

4.3.2. 1D nanostructures

1D nanostructures, including nanowires, nanorods, and nanotubes, enable directional charge transport with minimal energy loss [160]. Their unique structural features promote efficient O_3 adsorption and rapid surface reactions, enhancing sensor performance [161]. Catto et al. [162] fabricated highly oriented α-Fe_2O_3 nanorod arrays on an Al_2O_3 substrate with Pt interdigitated electrodes. They exhibited a low detection limit (15 ppb) (Fig. 12a) and high selectivity at 150 °C (Fig. 12b). Lai et al. [86] prepared CuO nanowires on Si (100) substrates via thermal oxidation (Fig. 12c). The as-fabricated sensor exhibited a 40% response to 50 ppb O_3 at 100 °C (Fig. 12d), substantially exceeding unmodified a-IGZO films. Notably, the O_3 response exhibited a clear positive correlation with nanowire length (Fig. 12e), highlighting the importance of morphological control for sensing performance optimization.

4.3.3. 2D nanostructures

2D nanostructures feature planar sheet-like morphologies that provide extensive surfaces for O_3 adsorption and diffusion. Their large surface areas facilitate rapid O_3 dispersion across the material, accelerating interactions with metal oxides and promoting electron transfer [163]. Ding et al. [164] fabricated hexagonal/orthogonal WO_3 homojunction nanosheets via hydrothermal synthesis. This structure increased the depletion layer thickness and facilitated carrier separation, promoting O_3 decomposition and significantly improving sensing performance (Fig. 13a). At 120 °C, the sensor achieved a response of 320.8 to 3.0 ppm O_3 (Fig. 13b), with a detection limit of 40 ppb. The layered structure enables multi-scale material integration, creating

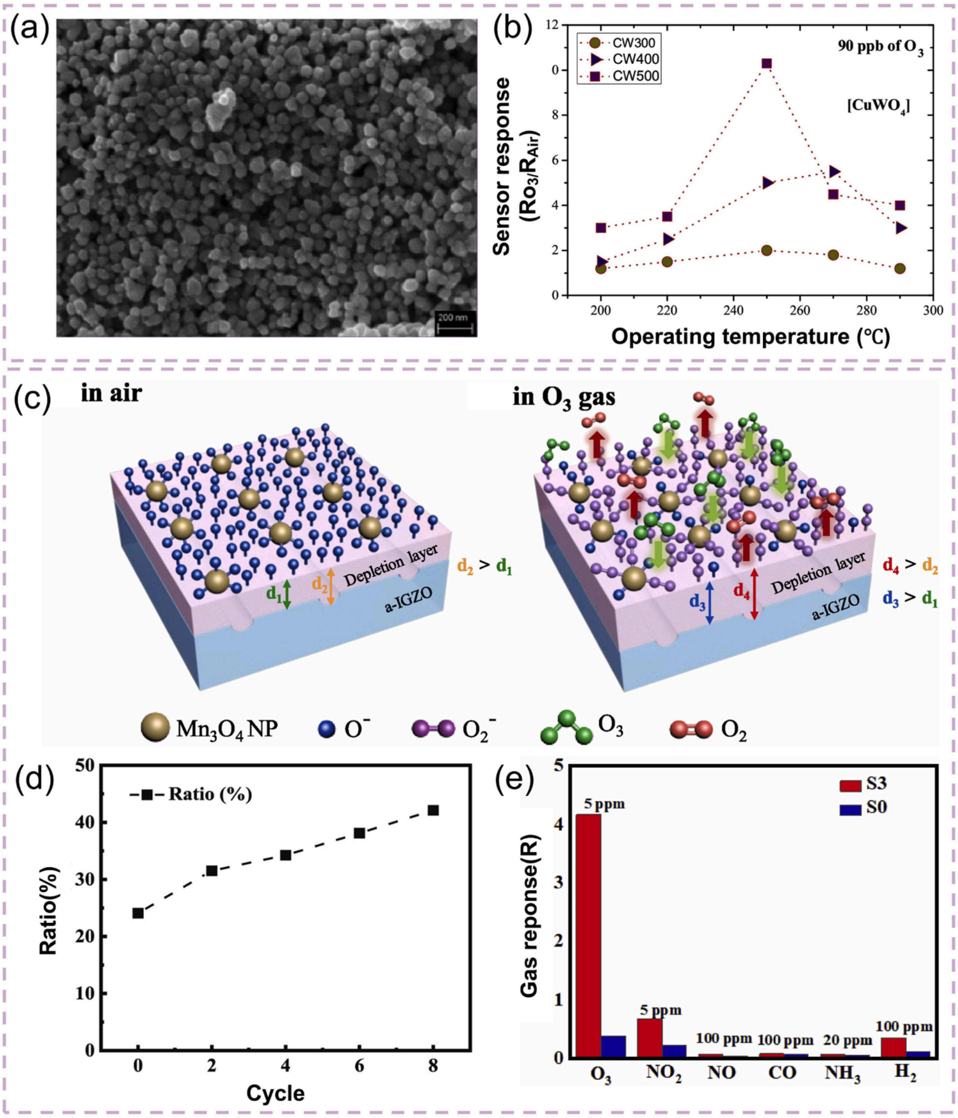

Fig. 10. (a) High magnification FE-SEM image of $CuWO_4$ sample annealed at 500 °C for 1 h. It presents a uniform morphology of nanoparticles. (b) Gas sensor's response of $CuWO_4$ samples exposed to 90 ppb O_3 at different operating temperatures. Reproduced with permission from Ref. [128], Copyright 2018 Elsevier. (c) Schematic illustrations of the gas sensor before (left) and after exposure (right) to O_3 gas. Relationship between soaking cycle and root mean square. Oxygen molecules adsorb on the a-IGZO thin film surface and extract free electrons, forming a surface depletion region with depth d_1. The attached p-type Mn_3O_4 nanoparticles (NPs) further capture electrons, increasing hole concentration and expanding the depletion region beneath them to d_2 ($d_2 > d_1$). When exposed to O_3, more electrons are withdrawn from the a-IGZO surface, deepening the depletion region to d_3 ($d_3 > d_1$). Due to the higher oxygen vacancy concentration in Mn_3O_4 NPs compared to a-IGZO, their depletion region can further expand to d_4 ($d_4 > d_2$). (d) The relationship between immersion cycles and the average area ratio of oxygen vacancy. (e) Selectivity of pristine a-IGZO film (S0) and Mn_3O_4 NPs decorated a-IGZO film (S3) for various target gases. Reproduced with permission from Ref. [156], Copyright 2024 Elsevier.

hierarchical systems optimized for O_3 adsorption, reaction, and charge conduction across micro-to-macro scales. It facilitates deep-layer O_3 interaction and ensures stable electrical signal output. Sui et al. [115] synthesized layered In_2O_3 nanosheets through a one-pot hydrothermal method followed by annealing treatment. The layered structure design can effectively increase the specific surface area of the material, up to a maximum of 60.6 m^2/g (Fig. 13c). At 80 °C, the sensor exhibited a response of 16.7 to 100 ppb O_3 (Fig. 13)), and the t_{res} and t_{rec} were 707 s and 422 s, respectively, at the background of air (Fig. 13e).

4.3.4. 3D nanostructures

3D nanostructures are constructed through hierarchical assembly of lower-dimensional units such as nanowires and nanosheets. Porous architectures are formed that simultaneously maximize surface interactions and optimize gas diffusion pathways [123]. Nagarjuna et al. [165] fabricated ZnO porous nanostructures through controlled annealing (Fig. 14a). The as-fabricated sensor films demonstrated a response of 32% to 50 ppb O_3 (Fig. 14b). Huang et al. [166] employed solution combustion synthesis to synthesize porous CuO nanoparticles with high surface areas (Fig. 14c). As the operating temperature decreases from 120 °C to 25 °C, the response increases due to the enhanced adsorption of O_3 gas (Fig. 14d).

Rational nanostructure design significantly enhances the performance of MOS-based O_3 sensors. By increasing the specific surface area and active site density, nanostructures facilitate O_3 adsorption and redox reactions. After critical microstructure parameters, such as dimension, porosity, and exposed crystal facets, are simultaneously optimized, O_3 interaction can be tailored for rapid and selective detection, even at trace concentrations.

To summarize, in this chapter, we have comprehensively

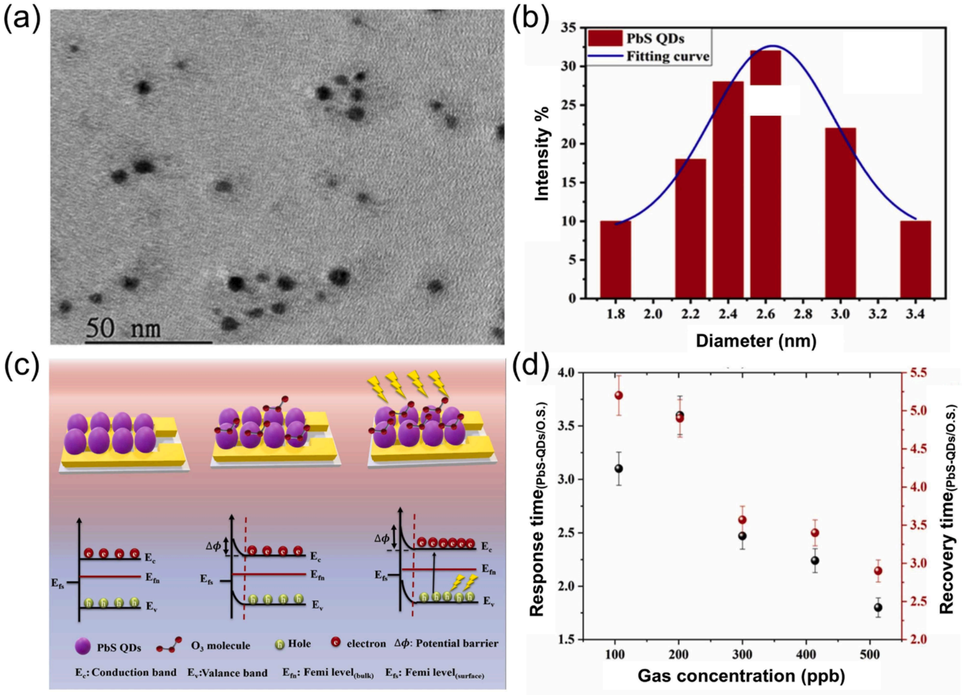

Fig. 11. (a) HRTEM analysis of PbS QDS at 50 nm scale. (b) Average particle size analysis. The particle sizes are distributed mainly around 2.7 nm. Most of the particle sizes range from 2.3 to 2.8 nm. (c) The gas sensing mechanism of photoactivated PbS QDs.When the 0D PbS has been exposed to air, oxygen molecules get adsorbed onto their surfaces, then the oxygen molecule gets ionized by capturing the ions from the surface of QDs, formation of the depletion layer and creating a potential barrier across the junction. As a result, the depletion layer starts decreasing, which increases the electrical conductivity. On exposure to O_3, the O_3 molecules get adsorbed on the junction and increase the depletion layer, which increases the potential barrier across them. When the PbS QDs were exposed to different light irradiations then holes were migrated from the valence band to the conduction band during oxygen species adsorption. (d) Comparison of the ratio of response and recovery time at different concentrations. Reproduced with permission from Ref. [159], Copyright 2022 Elsevier.

investigated the influence of MOS's chemical composition and nanoscale architecture on the O_3 sensing performances. Single-component MOS materials usually have inherent limitations due to insufficient gas adsorption and limited reaction sites. Elemental doping effectively modulates carrier concentrations, engenders oxygen vacancies, and tunes the bandgap energy, thereby enhancing electronic transport and surface reactivity. Additionally, composite structures and heterojunctions facilitate interfacial charge transfer and synergistic adsorption, significantly enhancing sensing responses. Nanoscale structural engineering strategies further boost O_3 adsorption and redox kinetics by increasing the density of accessible active sites.

5. Device architecture design of the MOS sensors

Sensor technology has undergone a gradual transformation from traditional sintered type, thick film type, and thin film type to miniaturized and flexible architectures. Traditional MOS-based O_3 sensors provide structural stability and reliable performance. They generally rely on rigid substrates and high-temperature treatment, which are unfavorable for miniaturization and integration, particularly within compact building environments and indoor air quality monitoring systems. With the development of micro-nano manufacturing technologies, micro-electro-mechanical systems (MEMS) have emerged. It retains the traditional thin films as the sensitive layer and achieves low power consumption, high sensitivity, and batch production through integrating micro-heating platforms, electrodes, and packaging systems. Flexible sensors further integrate deformable substrates with stretchable electrodes and gas-sensitive materials, promoting the evolution of sensors from rigid devices to wearable, deformable, and building-integrated platforms suitable for spatially constrained indoor applications [167].

5.1. Traditional MOS-based O_3 sensors

Traditional MOS-based O_3 sensors can be classified into chip-type (Fig. 15a) and tube-type (Fig. 15b) based on their configurations. Depending on the preparation process of the gas-sensitive membranes, they can be further divided into sintered type, thick film type, and thin film type.

Sintered MOS sensors are usually fabricated by pressing powder materials into a specific shape and then subjecting them to high-temperature sintering [168]. They possess relatively high strength and can enhance their resistance to environmental interference. Thick film MOS-based O_3 sensors are commonly fabricated using a screen printing technique [169]. While offering mechanical robustness and environmental stability, the thick film structure hampers gas diffusion, resulting in slower response and recovery times [170]. Under the intersection, thin film MOS sensors have been widely studied in recent years due to their compact size, ease of integration, miniaturization, and faster gas diffusion advantages [171–173]. Thin film MOS sensors are typically fabricated using techniques including physical vapor deposition (PVD), chemical vapor deposition (CVD), and drop coating to deposit ultra-thin MOS films on substrates [174–176]. They also operate at lower temperatures, making them ideal for high-precision detection, especially for low-concentration gases [177]. For instance, Huang et al. [178] deposited the sensing film on a glass substrate with gold electrodes using the radio frequency magnetron sputtering method. A self-powered a-IGZO thin film O_3 gas sensor was fabricated (Fig. 15c), which could respond to O_3 concentrations ranging from 100 ppb to 5 ppm (Fig. 15d).

5.2. MEMS sensors

The MEMS sensor is generally composed of three main components: the micro-heating plate, test electrodes, and sensitive materials [179].

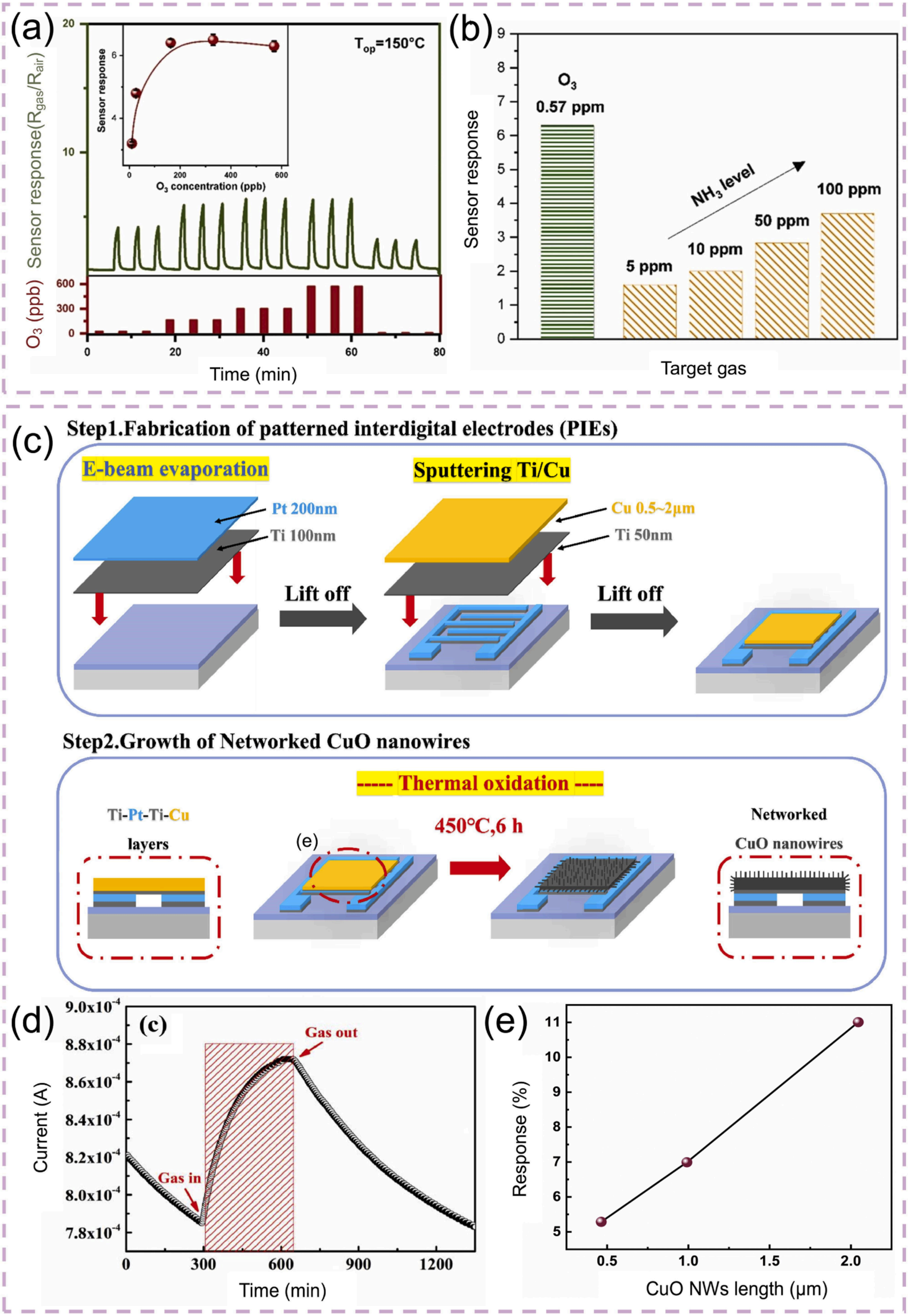

(caption on next page)

Fig. 12. (a) Dynamic response-recovery curves of α-Fe_2O_3 nanorods exposed to five different O_3 gas levels (26, 163, 300, 570 and 10 ppb) at 150 °C. The inset shows the sensing response as a function of O_3 gas concentration. (b) Sensor's responses to O_3 and NH_3 gases of α-Fe_2O_3 nanorods at 150 °C. Reproduced with permission from Ref. [162], Copyright 2023 Elsevier. (c) Schematic diagram of the manufacturing process of O_3 gas sensors based on CuO NWs. (d) Gas sensor's response of the 3.3 μm CuO NWs gas sensors exposed to 200 ppb O_3 at RT (25 °C). (e) The response of the O_3 gas sensor varies with the length of CuO NWs at a thermal oxidation temperature of 450 °C. Reproduced with permission from Ref. [86], Copyright 2024 Elsevier.

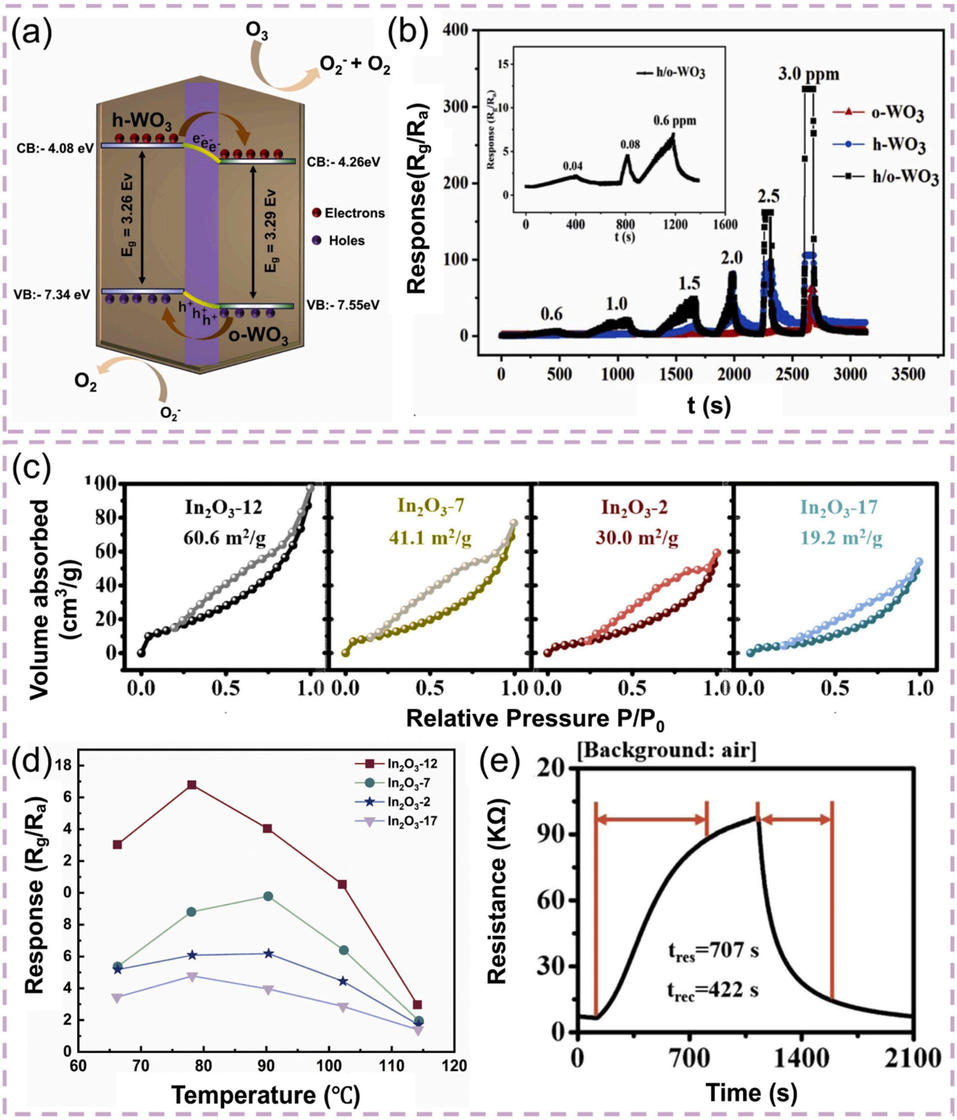

Fig. 13. (a) Schematic illustration of energy band diagram and O_3 sensing mechanism of h/o-WO_3 phase-junction sensors. The h/o-WO_3 homojunction enhances charge carrier separation at the phase interface, improving the decomposition of O_3 into oxygen on the material surface. Reproduced with permission from Ref. [164], Copyright 2025 Elsevier. (b) The response time curves of three WO_3 sensors to O_3 concentrations ranging from 0.6 to 3 ppm at 120 °C and the response time curves of h/o-WO_3 sensors to O_3 concentrations ranging from 0.04 to 0.6 ppm (the inset). (c) Nitrogen adsorption and desorption isotherms of In_2O_3 prepared at different hydrothermal times. (d) The responses of In_2O_3 prepared at different hydrothermal times to 100ppb O_3 at different operating temperatures. (e) Single dynamic sensing transients to 100 ppb of O_3. Reproduced with permission from Ref. [115], Copyright 2021 Elsevier.

Compared with traditional sensors, MEMS sensors achieve device miniaturization and significantly reduced energy consumption, making them ideal for space-constrained building environments and indoor air quality monitoring systems [180]. The existing MEMS-based micro-heater plate structures can be divided into two types: closed membrane type (Fig. 16a) and suspended membrane type, both enabling reliable operation in temperature-controlled indoor settings (Fig. 16b).

The closed-type structure, featuring a back-etched silicon substrate that forms a hollow structure with a micro-heating layer on it, offers excellent mechanical strength but results in higher energy consumption [181]. The suspended type uses front-end etching technology, retains the bottom structure, and suspends the micro-heating plate through four beams. This design achieves low energy consumption and a smaller heat conduction area at the expense of mechanical strength [182]. For instance, Nagarjuna et al. [183] fabricated a MEMS O_3 sensor using Sb/ZnO as the gas-sensitive material (Fig. 16c). The sensor exhibited optimal performance at an operating temperature of 200 °C, with a detection limit of 10 ppb for O_3, as shown in Fig. 16d. In addition, optimization of the MEMS micro-heating platform's design and manufacturing process achieved low heat loss, excellent long-term thermal stability, and robust mechanical stability [184,185]. As a typical example, Iyer et al. [186] explored various micro-heater

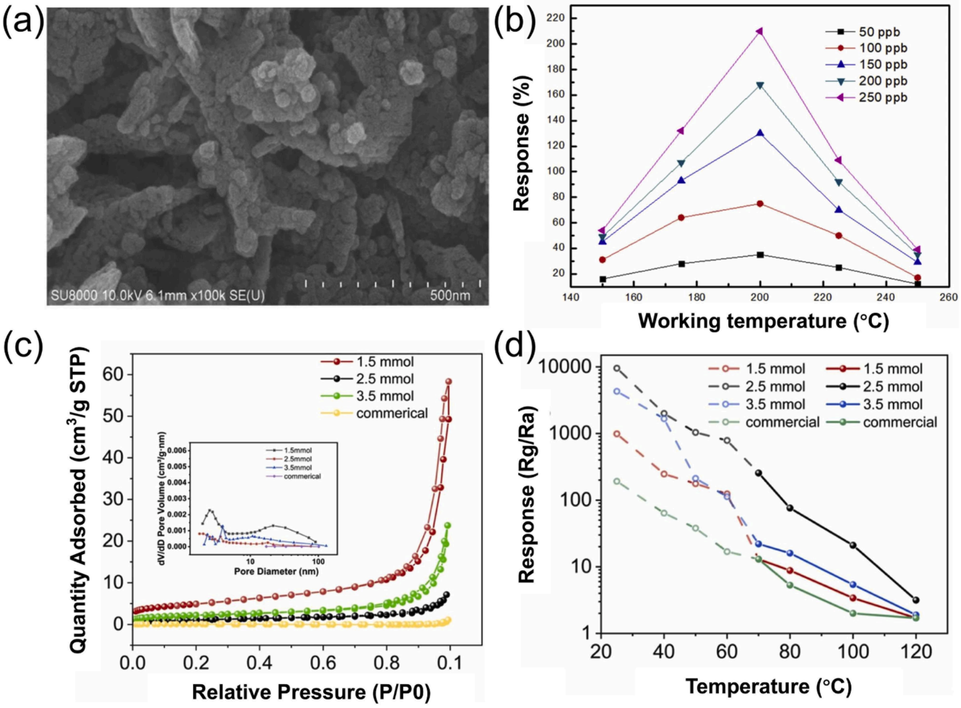

Fig. 14. (a) SEM images of Zn/ZnO samples. ZnO has a porous nanostructure. (b) Gas sensing responses of ZnO sensor with O_3 at different operating temperatures. Reproduced with permission from Ref. [165], Copyright 2013 Elsevier (c) Nitrogen adsorption and desorption isotherms of the CuO samples, the insert is the pore size distribution. (d) Response curves of the CuO sensors synthesized by different quantities of citric acid and commercial CuO powder to 500 ppb O_3 of samples synthesized from 3.5 mmol citric acid and commercially available CuO powder at an operating temperature of 25 to 120 °C. Reproduced with permission from Ref. [166], Copyright 2024 Elsevier.

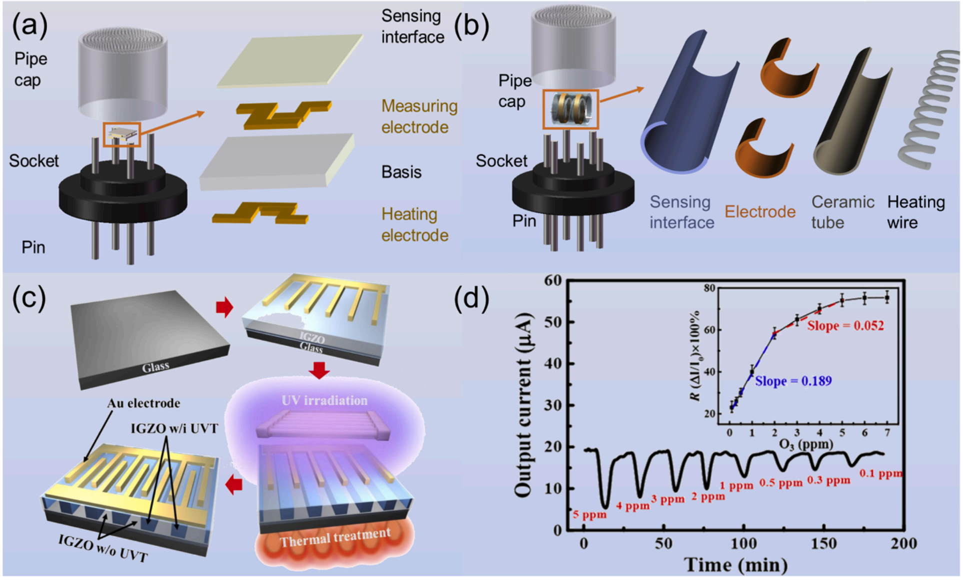

Fig. 15. (a) Structural diagram of chip-type MOS gas sensor. (b) Structure of the tube-type gas sensor. (c) Schematic diagram of the device manufacturing process of the Au/ a-IGZO/Au self-powered thin film gas sensor. (d) *I-T* curves of a self-powered a-IGZO gas sensor exposed to O_3 concentrations from 100 ppb to 5 ppm. Inset: *R* as a function of O_3 gas concentration. Reproduced with permission from Ref. [178], Copyright 2022 American Chemical Society.

structures (single meander, double meander, spiral, and meander-spiral) (Fig. 16e) to optimize the uniformity of temperature distribution and enhance O_3 adsorption efficiency. The results demonstrated that the meander-spiral geometric shape achieves the best temperature distribution uniformity across the sensor surface, thereby increasing the contact area of the sensor. This configuration exhibits a 4-fold sensitivity enhancement over the single meander design, and a 1.5-fold improvement compared to both double meander and spiral geometric shapes (Fig. 16f).

5.3. *Flexible sensors*

Flexible gas sensors have emerged as a promising solution to meet the rapidly growing industrial demand for intelligent wearable devices

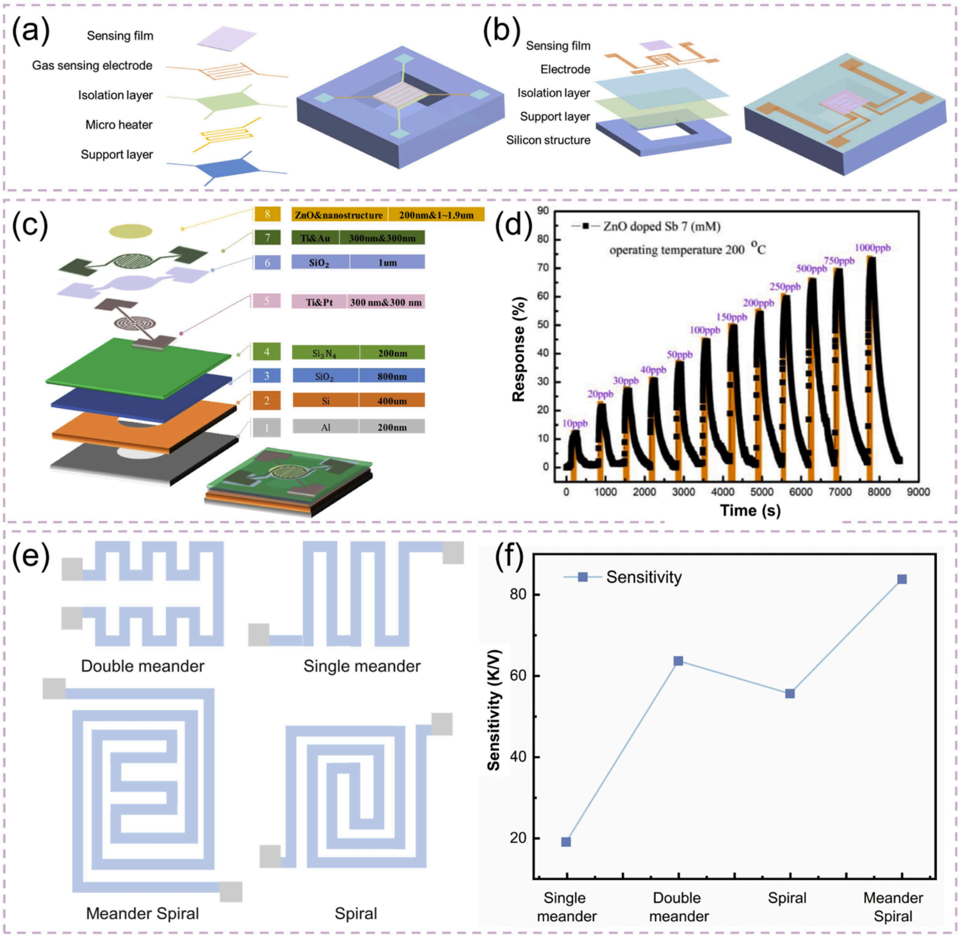

Fig. 16. (a) The structure of thin film MOS gas sensors of the closed type. (b) The structure of thin film MOS gas sensors of suspended type. (c) MEMS microheater design and layers. (d) Sb-doped ZnO sensor sensing responses. Reproduced with permission from Ref. [183], Copyright 2024 Elsevier. (e) The structural design of the miniature heater. (f) Comparison of the sensitivity of different structural MEMS sensors to O_3. Reproduced with permission from Ref. [186], Copyright 2022 Elsevier.

[187]. Compared to traditional gas sensors (Fig. 17a), flexible sensors (Fig. 17b) mainly use flexible substrate materials such as textile [188], paper [189], and polymeric substrates [190]. It addresses the brittleness limitation of traditional sensor rigid substrates, such as glass and silicon wafers [45,191,192].

Gas sensing materials are an important component of flexible gas

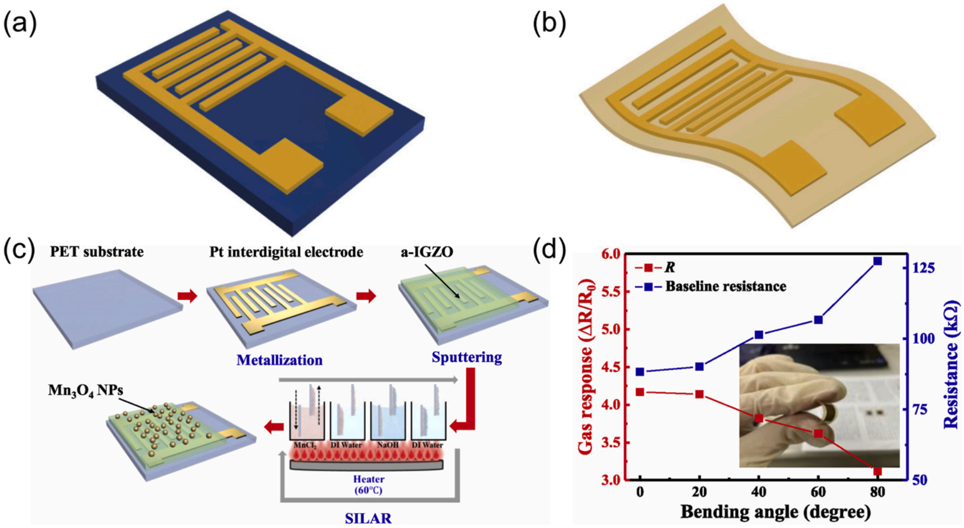

Fig. 17. (a) Schematic diagrams of conventional gas sensors. (b) Schematic diagrams of flexible gas sensors. Reproduced with permission from Ref. [192], Copyright 2023 Elsevier. (c) Schematic of the fabrication process for Mn_3O_4 NPs-decorated a-IGZO flexible gas sensors. (d) Gas response and device resistance as a function of bending angle. Inset of (d): image of a flexible gas sensor. Reproduced with permission from Ref. [156], Copyright 2024 Elsevier.

sensors. The sensing material, together with the flexible substrate, must withstand mechanical deformation. Even under bending or stretching, the sensing performance should exhibit minimal change [192]. Meanwhile, considering that many polymer-based flexible substrates lack heat tolerance, it is necessary to avoid high operating temperatures during the bonding process of the gas-sensitive material to the flexible substrate [193]. For instance, Tseng et al. [156] deposited Mn_3O_4 nanoparticles on the surface of an a-IGZO thin film with excellent mechanical properties as a gas-sensitive material. It addresses the technical concern that Mn_3O_4 nanoparticles require thermal bonding at high operating temperatures (Fig. 17c). Meanwhile, a polyethylene terephthalate (PET) film with finger-like Pt electrodes was used as the flexible substrate. It was found that the surface volume ratio and particle spacing of the gas-sensitive material changed with the bending angle of the sensor, resulting in changes in the baseline resistance of the material and the response to O_3. When the bending angle exceeded 40 degrees, the connectivity between a-IGZO grains was reduced. Consequently, the baseline resistance increased, and the response value decreased (Fig. 17d).

With the continuous progress of materials science, micro-nano manufacturing technology, and interdisciplinary integration research, the device structure of MOS-based O_3 sensors is continuously evolving from traditional thick film, thin film and sintered sensors to MEMS sensors and flexible sensors. The thin film and MEMS-type devices demonstrate outstanding performances in terms of response speed, energy consumption, and miniaturization, enabling seamless integration into building and indoor monitoring networks. And flexible sensors meet the urgent demands of emerging wearable and intelligent terminal devices for portability and real-time monitoring. Going forward, designing MOS-based O_3 sensor devices that are highly sensitive, use low power, and have a compact, integrated design while maintaining mechanical reliability for building environments and indoor applications will be a key focus of development.

6. Conclusion and prospects

Resistive MOS-based O_3 sensors have advanced significantly through the strategic integration of material design, nanostructural engineering, and environmental modulation. This review highlights how O_3 chemisorption, by driving both oxygen vacancy formation and charge transfer dynamics, underpins the high sensitivity and selectivity of MOS-based sensors at ppb levels. Doping strategies and heterojunction structures have proven essential for tailoring carrier concentrations and interfacial reactivity, enabling room-temperature operation with rapid response. Environmental factors, such as humidity-driven water dissociation and UV-light-activated photogenerated carriers, provide additional avenues to amplify sensor performance. However, achieving long-term operational stability and reducing power consumption in building-integrated and indoor applications remains challenging, mainly due to intrinsic material degradation and thermal management complexities in controlled building environments1. To address these issues, future research should explore the following avenues for innovation in MOS gas sensor technologies.

(1). **Materials innovation.** Future advances will depend on rationally designing hybrid structures that couple MOS with carbon-based nanomaterials, noble metals, or conductive polymer materials to achieve synergistic enhancements in surface area, charge mobility, and catalytic activity. Doping strategies and nanoscale structural engineering offer fine control over surface adsorption energetics, enabling faster response kinetics. In addition, the controlled synthesis of nanocrystals with well-defined morphology, particle size, and porosity can significantly increase the surface-to-volume ratio, providing more active sites for gas interactions.

(2). **Equipment manufacturing.** Deposition techniques including sol-gel, ALD, and magnetron sputtering can enhance the uniformity and repeatability of gas-sensitive materials on sensor substrates, reduce problems such as uneven material thickness, unstable interfaces, and poor repeatability caused by methods like drop coating and scrape coating, improve the consistency and reliability of devices, and lay the foundation for industrial applications. By simplifying the complexity of the deposition technology operation, the controllability and consistency of the manufacturing process can be further enhanced, enabling the batch and automated production of sensors.

(3). **Multifunctionality integration.** Integrating O_3 sensors into wearable and portable electronics is essential for enabling personalized, real-time monitoring of environmental O_3 exposure at occupant level in buildings and indoor spaces. Concurrent integration with O_3 sensors for other air pollutants (e.g., CO, NO_2, VOCs) will support the development of compact, multifunctional platforms capable of comprehensive air quality assessment for building-scale monitoring and indoor environmental management.

(4). **Intelligent system.** The confluence of Internet of Things (IoT) platforms and artificial intelligence algorithms provides a route toward autonomous sensing systems. Real-time data transmission, remote diagnostics, self-calibration, and anomaly recognition are becoming increasingly feasible through machine learning approaches in indoor environmental monitoring. Advanced pattern recognition and data fusion methodologies can further enhance multi-gas detection capabilities in building environments, fostering systems that respond dynamically to fluctuating environmental conditions with minimal human intervention.

Substantial advances have been made in the design, fabrication, and performance optimization of MOS-based O_3 sensors. However, the transition from laboratory prototypes to robust, field-ready devices for building-integrated deployment and indoor environmental monitoring remains a major challenge. A key barrier is the limited long-term stability of sensors operating under real-world building and indoor conditions. Factors such as fluctuations in operating temperature, humidity, oxygen concentrations, and mechanical stress from building operations can lead to degradation of sensor performance. The underlying mechanisms of material aging and device-level degradation in indoor environments remain insufficiently understood. Therefore, addressing these gaps will require systematic testing under controlled but variable environmental conditions to identify failure modes and guide the targeted improvements in material and device engineering for indoor deployment.

CRediT authorship contribution statement

Dongqing Pang: Writing – original draft, Resources. **Enze Tian:** Formal analysis, Conceptualization. **Ruijie Xie:** Writing – review & editing, Resources. **Ziquan Yin:** Visualization, Methodology. **Junquan Chen:** Visualization, Resources. **Jiaojiao Deng:** Writing – review & editing, Resources. **Jinhan Mo:** Writing – review & editing, Resources.

Declaration of competing interest

The authors declare that they have no known competing financial interests or personal relationships that could have appeared to influence the work reported in this paper.

Acknowledgment

This work was supported by the National Natural Science Foundation of China (Nos. 52325801, 52402052) and Shenzhen Natural Science

Foundation (No. JCYJ20240813143502004).

Data availability

No data was used for the research described in the article.

References

[1] M.Y. Wang, S.H.L. Yim, G.H. Dong, K.F. Ho, D.C. Wong, Mapping ozone source-receptor relationship and apportioning the health impact in the Pearl River Delta region using adjoint sensitivity analysis, Atmos. Environ. 222 (2020) 117026, https://doi.org/10.1016/j.atmosenv.2019.117026.

[2] Z. Chen, Q.W. Chen, Y. Wang, W.W. Zou, Y. Li, J.H. Mo, Tuning multi-scale pore structures in carbonaceous films via direct ink writing and sacrificial templates for efficient indoor formaldehyde removal, J. Hazard. Mater. 487 (2025) 137203, https://doi.org/10.1016/j.jhazmat.2025.137203.

[3] Z. Chen, E.Z. Tian, Y. Jiang, J.H. Mo, Global perspectives on indoor phthalates and alternative plasticizers: occurrence and key transport parameters, J. Hazard. Mater. 482 (2025) 136506, https://doi.org/10.1016/j.jhazmat.2024.136506.

[4] J.V. Santiago, H. Hata, E.J. Martinez-Noriega, K. Inoue, Ozone trends and their sensitivity in global megacities under the warming climate, Nat. Commun. 15 (1) (2024) 10236, https://doi.org/10.1038/s41467-024-54490-w.

[5] W. Chen, Y. Yang, H. Mei, H. Sun, P.K.K. Louie, S.Y. Jiang, Z. Ning, Analysis of an ozone episode in the Greater Bay Area based on low-cost sensor network, Atmos. Environ. 322 (2024) 120367, https://doi.org/10.1016/j.atmosenv.2024.120367.

[6] M. Wang, S. Li, R. Zhu, R. Zhang, L. Zu, Y. Wang, X. Bao, On-road tailpipe emission characteristics and ozone formation potentials of VOCs from gasoline, diesel and liquefied petroleum gas fueled vehicles, Atmos. Environ. 223 (2020) 117294, https://doi.org/10.1016/j.atmosenv.2020.117294.

[7] S. Li, G. Song, J. Xing, J. Dong, M. Zhang, C. Fan, S. Meng, J. Yang, L. Dong, W. Gong, Unraveling overestimated exposure risks through hourly ozone retrievals from next-generation geostationary satellites, Nat. Commun. 16 (1) (2025) 3364, https://doi.org/10.1038/s41467-025-58652-2.

[8] D.A. Malashock, M.N. DeLang, J.S. Becker, M.L. Serre, J.J. West, K.L. Chang, O. R. Cooper, S.C. Anenberg, Estimates of ozone concentrations and attributable mortality in urban, peri-urban and rural areas worldwide in 2019, Environ. Res. Lett. 17 (5) (2022) 054023, https://doi.org/10.1088/1748-9326/ac66f3.

[9] M. Brauer, G.A. Roth, A.Y. Aravkin, Global burden and strength of evidence for 88 risk factors in 204 countries and 811 subnational locations, 1990-2021: a systematic analysis for the Global Burden of Disease Study 2021, Lancet 403 (10440) (2024) 2162–2203, https://doi.org/10.1016/S0140-6736(24)00933-4.

[10] Y. Wang, Y. Yang, Q. Yuan, T. Li, Y. Zhou, L. Zong, M. Wang, Z. Xie, H.C. Ho, M. Gao, S. Tong, S. Lolli, L. Zhang, Substantially underestimated global health risks of current ozone pollution, Nat. Commun. 16 (1) (2025) 102, https://doi.org/10.1038/s41467-024-55450-0.

[11] L.D. Emberson, H. Pleijel, E.A. Ainsworth, M. van den Berg, W. Ren, S. Osborne, G. Mills, D. Pandey, F. Dentener, P. Büker, F. Ewert, R. Koeble, R. Van Dingenen, Ozone effects on crops and consideration in crop models, Eur. J. Agron. 100 (2018) 19–34, https://doi.org/10.1016/j.eja.2018.06.002.

[12] N.I. Mohammed, N.A. Ramli, A.S. Yahya, Ozone phytotoxicity evaluation and prediction of crops production in tropical regions, Atmos. Environ. 68 (2013) 343–349, https://doi.org/10.1016/j.atmosenv.2012.09.010.

[13] E. Agathokleous, P. Sicard, Z. Feng, E. Paoletti, Ozone pollution threatens bird populations to collapse: an imminent ecological threat? J. For. Res. 34 (6) (2023) 1653–1656, https://doi.org/10.1007/s11676-023-01645-y.

[14] E. Agathokleous, Z. Feng, E. Oksanen, P. Sicard, Q. Wang, C.J. Saitanis, V. Araminiene, J.D. Blande, F. Hayes, V. Calatayud, M. Domingos, S. D. Veresoglou, J. Peñuelas, D.A. Wardle, A. De Marco, Z. Li, H. Harmens, X. Yuan, M. Vitale, E. Paoletti, Ozone affects plant, insect, and soil microbial communities: a threat to terrestrial ecosystems and biodiversity, Sci. Adv. 6 (33) (2020) 1176, https://doi.org/10.1126/sciadv.abc1176.

[15] T. Grøntoft, K. Hallett, N. Blades, Environmental dose-response functions of silk and paper exposed in museums, Polym. Degrad. Stab. 227 (2024) 110878, https://doi.org/10.1016/j.polymdegradstab.2024.110878.

[16] S.A. Hawra, A.H. Bassam, Review of museums' indoor environment conditions studies and guidelines and their impact on the museums' artifacts and energy consumption, Build. Environ. 143 (2018) 186–195, https://doi.org/10.1016/j.buildenv.2018.07.012.

[17] D. Rim, E.T. Gall, R.L. Maddalena, W.W. Nazaroff, Ozone reaction with interior building materials: influence of diurnal ozone variation, temperature and humidity, Atmos. Environ. 125 (2016) 15–23, https://doi.org/10.1016/j.atmosenv.2015.10.093.

[18] K. Li, D.J. Jacob, L. Shen, X. Lu, I. De Smedt, H. Liao, Increases in surface ozone pollution in China from 2013 to 2019: anthropogenic and meteorological influences, Atmos. Chem. Phys. 20 (19) (2020) 11423–11433, https://doi.org/10.5194/acp-20-11423-2020.

[19] X. Lu, L. Zhang, X.L. Wang, M. Gao, K. Li, Y.Z. Zhang, X. Yue, Y.H. Zhang, Rapid increases in warm-season surface ozone and resulting health impact in China since 2013, Environ. Sci. Technol. Lett. 7 (4) (2020) 240–247, https://doi.org/10.1021/acs.estlett.0c00171.

[20] W. Wang, D.D. Parrish, S. Wang, F. Bao, R. Ni, X. Li, S. Yang, H. Wang, Y. Cheng, H. Su, Long-term trend of ozone pollution in China during 2014-2020: distinct seasonal and spatial characteristics and ozone sensitivity, Atmos. Chem. Phys. 22 (13) (2022) 8935–8949, https://doi.org/10.5194/acp-22-8935-2022.

[21] H.Z. Sun, K.R.V. Daalen, L. Morawska, S. Guillas, C. Giorio, Q. Di, H.D. Kan, E.X. L. Loo, L.P. Shek, N. Watts, Y.M. Guo, A.T. Archibald, An estimate of global cardiovascular mortality burden attributable to ambient ozone exposure reveals urban-rural environmental injustice, One Earth 7 (10) (2024) 1803–1819, https://doi.org/10.1016/j.oneear.2024.08.018.

[22] J.J. Wargent, B.R. Jordan, From ozone depletion to agriculture: understanding the role of UV radiation in sustainable crop production, New Phytol. 197 (4) (2013) 1058–1076, https://doi.org/10.1111/nph.12132.

[23] S. Chirumbolo, L. Valdenassi, S. Pandol, U. Tirelli, M. Franzini, Medical use of adjunct oxygen-ozone therapy and its impact on the scientific literature to date, Lancet Reg. Health Am. 35 (2024) 100807, https://doi.org/10.1016/j.lana.2024.100807.

[24] M. Franzini, U. Tirelli, L. Valdenassi, F. Vaiano, A.C. Galoforo, G. Ricevuti, S. Chirumbolo, Oxygen-ozone therapy in the medical sciences. State of art, Int. Immunopharmacol. 137 (112489) (2024) 112489, https://doi.org/10.1016/j.intimp.2024.112489.

[25] M.M. Iqbal, G. Muhammad, M.A. Hussain, H. Hanif, M.A. Raza, Z. Shafiq, Recent trends in ozone sensing technology, Anal. Methods 15 (23) (2023) 2798–2822, https://doi.org/10.1039/d3ay00334e.

[26] L. Petani, L. Koker, J. Herrmann, V. Hagenmeyer, U. Gengenbach, C. Pylatiuk, Recent developments in ozone sensor technology for medical applications, Micromachines 11 (6) (2020) 624, https://doi.org/10.3390/mi11060624.

[27] C. Grasso, V. Eramo, M. Lembo, R. Forniti, C. Carboni, R. Botondi, Effects of gaseous ozone treatment on the mite pest control and qualitative properties during ripening storage of pecorino cheese, J. Sci. Food Agric. 103 (4) (2023) 2124–2133, https://doi.org/10.1002/jsfa.12400.

[28] X.B. Pang, M.D. Shaw, A.C. Lewis, L.J. Carpenter, T. Batchellier, Electrochemical ozone sensors: a miniaturised alternative for ozone measurements in laboratory experiments and air-quality monitoring, Sens. Actuators B 240 (2017) 829–837, https://doi.org/10.1016/j.snb.2016.09.020.

[29] R. Baron, J. Saffell, Amperometric gas sensors as a low cost emerging technology platform for air quality monitoring applications: a review, ACS Sens. 2 (11) (2017) 1553–1566, https://doi.org/10.1021/acssensors.7b00620.

[30] A. Abbasi, J.J. Sardroodi, Investigation of the adsorption of ozone molecules on TiO_2/WSe_2 nanocomposites by DFT computations: applications to gas sensor devices, Appl. Surf. Sci. 436 (2018) 27–41, https://doi.org/10.1016/j.apsusc.2017.12.010.

[31] Y. Li, M. Dvořák, P.N. Nesterenko, N. Nuchtavorn, M. Macka, High power deep UV-LEDs for analytical optical instrumentation, Sens. Actuators B 255 (2018) 1238–1243, https://doi.org/10.1016/j.snb.2017.08.085.

[32] M.S. Xu, L. Liu, W. Tian, Y. Xu, J.F. Tao, Development of a nonresonant photoacoustic gas sensor for ozone detection, IEEE Sens. J. 24 (21) (2024) 35508–35515, https://doi.org/10.1109/Jsen.2024.3459898.

[33] P.J.D. Peterson, A. Aujla, K.H. Grant, A.G. Brundle, M.R. Thompson, J. Vande Hey, R.J. Leigh, Practical use of metal oxide semiconductor gas sensors for measuring nitrogen dioxide and ozone in urban environments, Sensors 17 (7) (2017) 1653, https://doi.org/10.3390/s17071653.

[34] P. Wei, Z. Ning, S. Ye, L. Sun, F.H. Yang, K.C. Wong, D. Westerdahl, P.K.K. Louie, Impact analysis of temperature and humidity conditions on electrochemical sensor response in ambient air quality monitoring, Sensors 18 (2) (2018) 59, https://doi.org/10.3390/s18020059.

[35] S. Palzer, Photoacoustic-based gas sensing: a review, Sensors 20 (9) (2020) 2745, https://doi.org/10.3390/s20092745.

[36] N.A. Isaac, I. Pikaar, G. Biskos, Metal oxide semiconducting nanomaterials for air quality gas sensors: operating principles, performance, and synthesis techniques, Mikrochim. Acta 189 (5) (2022) 196, https://doi.org/10.1007/s00604-022-05254-0.

[37] L. Zhu, W. Zeng, Room-temperature gas sensing of ZnO-based gas sensor: a review, Sens. Actuators A 267 (2017) 242–261, https://doi.org/10.1016/j.sna.2017.10.021.

[38] C. Zhang, Y. Luo, J. Xu, M. Debliquy, Room temperature conductive type metal oxide semiconductor gas sensors for NO_2 detection, Sens. Actuators A 289 (2019) 118–133, https://doi.org/10.1016/j.sna.2019.02.027.

[39] S. Wang, Y. Yang, X. Li, T. Wang, J. Li, G. Shi, G. Wang, Room temperature solid electrolyte ozone sensor based on Ag-doped SnO_2, Sens. Actuators A 365 (2024) 114915, https://doi.org/10.1016/j.sna.2023.114915.

[40] Y. Tian, J.X. Li, X. Li, R.Q. Wang, Y.R. Zhang, W.P. Chen, K. Song, G.Y. Wang, G. F. Shi, ZIF-8/ZIF-67 solid electrolyte ozone sensor at room temperature, Sens. Actuators A 354 (2023) 114281, https://doi.org/10.1016/j.sna.2023.114281.

[41] P.C. Andersen, C.J. Williford, J.W. Birks, Miniature personal ozone monitor based on UV absorbance, Anal. Chem. 82 (19) (2010) 7924–7928, https://doi.org/10.1021/ac1013578.

[42] T.C.E. Marcus, M.H. Ibrahim, N.H. Ngajikin, A.I. Azmi, Optical path length and absorption cross section optimization for high sensitivity ozone concentration measurement, Sens. Actuators B 221 (2015) 570–575, https://doi.org/10.1016/j.snb.2015.07.005.

[43] Y. Meng, R. Han, H. Wan, Z. Wang, Z. Du, A miniaturized photometric ozone sensor using ultraviolet LED with unbalance differential correction and 3D printing, Spectrochim. Acta Part A 304 (2024) 123335, https://doi.org/10.1016/j.saa.2023.123335.

[44] K. Keeratirawee, P.C. Hauser, Photoacoustic detection of ozone with a red laser diode, Talanta 223 (2021) 121890, https://doi.org/10.1016/j.talanta.2020.121890.

[45] L.X. Ou, M.Y. Liu, L.Y. Zhu, D.W. Zhang, H.L. Lu, Recent progress on flexible room-temperature gas sensors based on metal oxide semiconductor, Nano Micro Lett. 14 (1) (2022) 206, https://doi.org/10.1007/s40820-022-00956-9.

[46] S. Das, S. Mojumder, D. Saha, M. Pal, Influence of major parameters on the sensing mechanism of semiconductor metal oxide based chemiresistive gas sensors: a review focused on personalized healthcare, Sens. Actuators B 352 (2022) 131066, https://doi.org/10.1016/j.snb.2021.131066.

[47] L.Y. Gai, R.P. Lai, X.H. Dong, X. Wu, Q.T. Luan, J. Wang, H.F. Lin, W.H. Ding, G. L. Wu, W.F. Xie, Recent advances in ethanol gas sensors based on metal oxide semiconductor heterojunctions, Rare Met. 41 (6) (2022) 1818–1842, https://doi.org/10.1007/s12598-021-01937-4.

[48] Z. Li, Z. Lin, N. Wang, Y. Huang, J. Wang, W. Liu, Y. Fu, Z. Wang, Facile synthesis of α-Fe_2O_3 micro-ellipsoids by surfactant-free hydrothermal method for sub-ppm level H_2S detection, Mater. Des. 110 (2016) 532–539, https://doi.org/10.1016/j.matdes.2016.08.035.

[49] V.A. Lavrenko, I.A. Podchernyaeva, D.V. Shchur, A.D. Zolotarenko, A. D. Zolotarenko, Features of physical and chemical adsorption during interaction of polycrystalline and nanocrystalline materials with gases, Powder Metall. Met. Ceram. 56 (9–10) (2018) 504–511, https://doi.org/10.1007/s11106-018-9922-z.

[50] X. Meng, Y. Ren, Y. Zhou, J. Guo, L. Zhang, C. Qi, B. Liu, H. Yang, S. Liu, Fe_3O_4 nano-octahedral Fe-Fe_3O_4 (1 1 1) polar surface coordinated Fe atom enhanced sensing properties and its sensing atomic mechanism, Appl. Surf. Sci. 623 (2023) 156999, https://doi.org/10.1016/j.apsusc.2023.156999.

[51] Z. Zhang, J. Ma, W. Hou, H. Zhai, H. Yong, J. Hu, K. Zhang, Y. Zhang, H. Wang, J. Liu, Amorphous metal-organic frameworks-derived In_2O_3 microstructures with abundant oxygen vacancies for superior chlorine gas sensing performance, Sens. Actuators B 426 (2025) 137072, https://doi.org/10.1016/j.snb.2024.137072.

[52] C. Zhang, G. Liu, X. Geng, K. Wu, M. Debliquy, Metal oxide semiconductors with highly concentrated oxygen vacancies for gas sensing materials: a review, Sens. Actuators A 309 (2020) 112026, https://doi.org/10.1016/j.sna.2020.112026.

[53] P. Wang, X. Feng, J. Liang, J. Zhang, T. Niu, L. Li, Dual-site engineering of Au/Sr-ZnO photocatalysts for lattice oxygen-activated methane coupling to ethane with high selectivity, Appl. Catal. B Environ. 375 (2025) 125437, https://doi.org/10.1016/j.apcatb.2025.125437.

[54] N. Khomarloo, E. Mohsenzadeh, H. Gidik, R. Bagherzadeh, M. Latifi, Overall perspective of electrospun semiconductor metal oxides as high-performance gas sensor materials for NO_x detection, RSC Adv. 14 (11) (2024) 7806–7824, https://doi.org/10.1039/d3ra08119b.

[55] X. Zhou, Z. Xue, X. Chen, C. Huang, W. Bai, Z. Lu, T. Wang, Nanomaterial-based gas sensors used for breath diagnosis, J. Mater. Chem. B 8 (16) (2020) 3231–3248, https://doi.org/10.1039/c9tb02518a.

[56] B.X. Yang, N.V. Myung, T.T. Tran, 1D metal oxide semiconductor materials for chemiresistive gas sensors: a review, Adv. Electron. Mater. 7 (9) (2021) 2100271, https://doi.org/10.1002/aelm.202100271.

[57] S. Uma, M.K. Shobana, Band structure and mechanism of semiconductor metal oxide heterojunction gas sensor, Inorg. Chem. Commun. 160 (2024) 111941, https://doi.org/10.1016/j.inoche.2023.111941.

[58] N. Barsan, C. Simion, T. Heine, S. Pokhrel, U. Weimar, Modeling of sensing and transduction for p-type semiconducting metal oxide based gas sensors, J. Electroceram. 25 (1) (2009) 11–19, https://doi.org/10.1007/s10832-009-9583-x.

[59] H. Liu, J. Wan, Q. Fu, M. Li, W. Luo, Z. Zheng, H. Cao, Y. Hu, D. Zhou, Tin oxide films for nitrogen dioxide gas detection at low temperatures, Sens. Actuators B 177 (2013) 460–466, https://doi.org/10.1016/j.snb.2012.11.051.

[60] Y.K. Gautam, K. Sharma, S. Tyagi, A.K. Ambedkar, M. Chaudhary, B. Pal Singh, Nanostructured metal oxide semiconductor-based sensors for greenhouse gas detection: progress and challenges, R. Soc. Open Sci. 8 (3) (2021) 201324, https://doi.org/10.1098/rsos.201324.

[61] X. Liu, S.T. Cheng, H. Liu, S. Hu, D.Q. Zhang, H.S. Ning, A survey on gas sensing technology, Sensors 12 (7) (2012) 9635–9665, https://doi.org/10.3390/s120709635.

[62] V.E. Bochenkov, G.B. Sergeev, Sensitivity, selectivity, and stability of gas-sensitive metal-oxide nanostructures, Sci. Am. (2010) 31–52.

[63] H. Chai, Z. Zheng, K. Liu, J. Xu, K. Wu, Y. Luo, H. Liao, M. Debliquy, C. Zhang, Stability of metal oxide semiconductor gas sensors: a review, IEEE Sens. J. 22 (6) (2022) 5470–5481, https://doi.org/10.1109/jsen.2022.3148264.

[64] A. Nanda, V. Singh, R.K. Jha, J. Sinha, S. Avasthi, N. Bhat, Growth-temperature dependent unpassivated oxygen bonds determine the gas sensing abilities of chemical vapor deposition-grown CuO thin films, ACS Appl. Mater. Interfaces 13 (18) (2021) 21936–21943, https://doi.org/10.1021/acsami.1c01085.

[65] K. Wu, C. Zhang, Facile synthesis and ppb-level H_2S sensing performance of hierarchical CuO microflowers assembled with nano-spindles, J. Mater. Sci. Mater. Electron. 31 (10) (2020) 7937–7945, https://doi.org/10.1007/s10854-020-03332-8.

[66] S. Vallejos, I. Grácia, O. Chmela, E. Figueras, J. Hubálek, C. Cané, Chemoresistive micromachined gas sensors based on functionalized metal oxide nanowires: performance and reliability, Sens. Actuators B 235 (2016) 525–534, https://doi.org/10.1016/j.snb.2016.05.102.

[67] Z. Zhang, C. Jia, T. Li, C. Zhang, P. Li, B. Tian, X. Tian, H. Wang, Z. Tan, Z. Luo, A solution to cross-sensitivity - skeptics of traditional selectivity for MOS sensors under complex multi-component gases in transformer DGA, Sens. Actuators B 424 (2025) 136914, https://doi.org/10.1016/j.snb.2024.136914.

[68] M.R. Tchalala, P.M. Bhatt, K.N. Chappanda, S.R. Tavares, K. Adil, Y. Belmabkhout, A. Shkurenko, A. Cadiau, N. Heymans, G. De Weireld, G. Maurin, K.N. Salama, M. Eddaoudi, Fluorinated MOF platform for selective removal and sensing of SO_2 from flue gas and air, Nat. Commun. 10 (1) (2019) 1328, https://doi.org/10.1038/s41467-019-09157-2.

[69] G. Korotcenkov, Metal oxides for solid-state gas sensors: what determines our choice? Mater. Sci. Eng. B Adv. 139 (1) (2007) 1–23, https://doi.org/10.1016/j.mseb.2007.01.044.

[70] M. Wusiman, F. Taghipour, Methods and mechanisms of gas sensor selectivity, Crit. Rev. Solid State Mater. Sci. 47 (3) (2021) 416–435, https://doi.org/10.1080/10408436.2021.1941752.

[71] P.M. Bulemo, D.H. Kim, H. Shin, H.J. Cho, W.T. Koo, S.J. Choi, C. Park, J. Ahn, A. T. Guntner, R.M. Penner, I.D. Kim, Selectivity in chemiresistive gas sensors: strategies and challenges, Chem. Rev. 125 (8) (2025) 4111–4183, https://doi.org/10.1021/acs.chemrev.4c00592.

[72] M.I.S. Veríssimo, A critical review of the analytical performance of the most recent MOS-based gas sensors for indoor air quality monitoring of WHO priority pollutants, TrAC Trends Anal. Chem. 178 (2024) 117813, https://doi.org/10.1016/j.trac.2024.117813.

[73] L. Zhang, M. Zhou, F. Meng, J. Bai, D. Wang, M. Tang, Z. Wu, Recent advances in chemiresistive gas sensor for acetone detection: focus on room temperature, TrAC Trends Anal. Chem. 187 (2025) 118213, 10.1016/j.trac.2025.118213.

[74] J. Ding, Z. Li, Y. Wang, Y. Liu, F. Li, X. Yu, P. Huang, Y. Wang, Ir doping improved oxygen activation of WO_3 for boosting acetone sensing performance at low working temperature, Appl. Surf. Sci. 679 (2025) 161239, https://doi.org/10.1016/j.apsusc.2024.161239.

[75] R. Thayil, S.R. Parne, Recent advances and prospects on MoX_2 (X=S, Se, Te) nanostructure-based sensors for room temperature gas detection: a review, Surf. Interfaces 52 (2024) 104966, https://doi.org/10.1016/j.surfin.2024.104966.

[76] S. Kumar, A. Mirzaei, A. Kumar, M. Hoon Lee, Z. Ghahremani, T.U. Kim, J.Y. Kim, M. Kwoka, M. Kumar, S. Sub Kim, H. Woo Kim, Nanoparticles anchored strategy to develop 2D MoS_2 and $MoSe_2$ based room temperature chemiresistive gas sensors, Coord. Chem. Rev. 503 (2024) 215657, https://doi.org/10.1016/j.ccr.2024.215657.

[77] L. Shao, Z. Wu, H. Duan, T. Shaymurat, Discriminative and rapid detection of ozone realized by sensor array of Zn^{2+} doping tailored MoS_2 ultrathin nanosheets, Sens. Actuators B 258 (2018) 937–946, https://doi.org/10.1016/j.snb.2017.11.166.

[78] L. Liu, T. Li, Z. Yi, F. Chi, Z. Lin, X. Zhang, K. Xu, Conductometric ozone sensor based on mesoporous ultrafine Co_3O_4 nanobricks, Sens. Actuators B 297 (2019) 126815, https://doi.org/10.1016/j.snb.2019.126815.

[79] F.H. Saboor, T. Ueda, K. Kamada, T. Hyodo, Y. Mortazavi, A.A. Khodadadi, Y. Shimizu, Enhanced NO_2 gas sensing performance of bare and Pd-loaded SnO_2 thick film sensors under UV-light irradiation at room temperature, Sens. Actuators B 223 (2016) 429–439, https://doi.org/10.1016/j.snb.2015.09.075.

[80] T. Ueda, H. Abe, K. Kamada, S.R. Bishop, H.L. Tuller, T. Hyodo, Y. Shimizu, Enhanced sensing response of solid-electrolyte gas sensors to toluene: role of composite Au/metal oxide sensing electrode, Sens. Actuators B 252 (2017) 268–276, https://doi.org/10.1016/j.snb.2017.05.172.

[81] D. Zhang, Z. Yang, P. Li, X. Zhou, Ozone gas sensing properties of metal-organic frameworks-derived In_2O_3 hollow microtubes decorated with ZnO nanoparticles, Sens. Actuators B 301 (2019) 127081, https://doi.org/10.1016/j.snb.2019.127081.

[82] G. Korotcenkov, I. Blinov, V. Brinzari, J.R. Stetter, Effect of air humidity on gas response of SnO_2 thin film ozone sensors, Sens. Actuators B 122 (2) (2007) 519–526, https://doi.org/10.1016/j.snb.2006.06.025.

[83] Z. Jin, J. Zhao, L. Liu, F. Liu, Z. Wang, F. Wang, J. Liu, Y. Mou, L. Wu, X. Wu, Humidity-independent gas sensors in the detection of hydrogen sulfide based on Nd_2O_3-loaded In_2O_3 porous nanorods, Sens. Actuators B 403 (2024) 135237, https://doi.org/10.1016/j.snb.2023.135237.

[84] Z. Liang, M. Wang, S. Liu, X. Zhang, G. Liu, G. Qiao, Au-Pt nanoclusters decorated WS_2 nanosheets for achieving highly sensitive NO_2 sensing at room temperature, Chem. Eng. J. 495 (2024) 153703, https://doi.org/10.1016/j.cej.2024.153703.

[85] Z. Zhu, J.L. Chang, C.H. Wu, T.L. Chou, R.J. Wu, Promotion effect of silver on indium(III) oxide for detecting trace amounts of ozone, Sens. Actuators B 232 (2016) 442–447, https://doi.org/10.1016/j.snb.2016.03.088.

[86] L.T. Lai, H.T. Hsueh, C.H. Chiu, T.C. Cheng, S.J. Chang, Thermal oxidation CuO nanowire gas sensor for ozone detection applications, Sens. Actuators Rep. 8 (2024) 100228, https://doi.org/10.1016/j.snr.2024.100228.

[87] C. Esteves, S.I.C.J. Palma, H.M.A. Costa, C. Alves, G.M.C. Santos, E. Ramou, A. L. Carvalho, V. Alves, A.C.A. Roque, Tackling humidity with designer ionic liquid-based gas sensing soft materials, Adv. Mater. 34 (8) (2022) 2107205, https://doi.org/10.1002/adma.202107205.

[88] T. Wagner, J. Hennemann, C.D. Kohl, M. Tiemann, Photocatalytic ozone sensor based on mesoporous indium oxide: influence of the relative humidity on the sensing performance, Thin Solid Films 520 (3) (2011) 918–921, https://doi.org/10.1016/j.tsf.2011.04.181.

[89] M. Yang, J. Lu, X. Wang, H. Zhang, F. Chen, J. Sun, J. Yang, Y. Sun, G. Lu, Acetone sensors with high stability to humidity changes based on Ru-doped NiO flower-like microspheres, Sens. Actuators B 313 (2020) 127965, https://doi.org/10.1016/j.snb.2020.127965.

[90] S. Vallejos, I. Gràcia, N. Pizúrová, E. Figueras, J. Čechal, J. Hubálek, C. Cané, Gas sensitive ZnO structures with reduced humidity-interference, Sens. Actuators B 301 (2019) 127054, https://doi.org/10.1016/j.snb.2019.127054.

[91] Z. Zhu, J.L. Chang, R.J. Wu, Fast ozone detection by using a core-shell Au@TiO_2 sensor at room temperature, Sens. Actuators B 214 (2015) 56–62, https://doi.org/10.1016/j.snb.2015.03.017.

[92] J.M. Suh, T.H. Eom, S.H. Cho, T. Kim, H.W. Jang, Light-activated gas sensing: a perspective of integration with micro-LEDs and plasmonic nanoparticles, Mater. Adv. 2 (3) (2021) 827–844, https://doi.org/10.1039/d0ma00685h.

[93] J.V.N. de Palma, A.C. Catto, M.C. de Oliveira, R.A.P. Ribeiro, M.D. Teodoro, L. F. da Silva, Light-assisted ozone gas-sensing performance of SnO_2 nanoparticles: experimental and theoretical insights, Sens. Actuators Rep. 4 (2022) 100081, https://doi.org/10.1016/j.snr.2022.100081.

[94] C.H. Wu, K.W. Chang, Y.N. Li, Z.Y. Deng, K.L. Chen, C.C. Jeng, R.J. Wu, J. H. Chen, Improving the sensitive and selective of trace amount ozone sensor on indium-gallium-zinc oxide thin film by ultraviolet irradiation, Sens. Actuators B 273 (2018) 1713–1718, https://doi.org/10.1016/j.snb.2018.07.075.

[95] C.Y. Huang, X.R. He, J.J. Jhang, J.H. Wu, T.H. Wu, T.Y. Lin, A self-powered dual-functional hybrid Cu_2O/SiNWs heterojunction with applications in broadband photodetectors and ozone gas sensors, Sens. Actuators A 347 (2022) 113992, https://doi.org/10.1016/j.sna.2022.113992.

[96] C.Y. Huang, C.Y. Yan, Y.Q. Lou, Dual-functional hybrid ZnSnO/graphene nanocomposites with applications in high-performance UV photodetectors and ozone gas sensors, Ceram. Int. 48 (3) (2022) 3527–3535, https://doi.org/10.1016/j.ceramint.2021.10.131.

[97] S. Thirumalairajan, K. Girija, V.R. Mastelaro, K.S. Subramanian, Enhanced ultrasensitive detection of ozone gas using reduced graphene oxide-incorporated $LaFeO_3$ nanospheres for environmental remediation process, J. Mater. Sci. Mater. Electron. 31 (11) (2020) 8933–8945, https://doi.org/10.1007/s10854-020-03428-1.

[98] J. Jayachandiran, M. Arivanandhan, O. Padmaraj, R. Jayavel, D. Nedumaran, Investigation on ozone-sensing characteristics of surface sensitive hybrid rGO/WO_3 nanocomposite films at ambient temperature, Adv. Compos. Hybrid Mater. 3 (1) (2020) 16–30, https://doi.org/10.1007/s42114-020-00134-8.

[99] M. Acuautla, S. Bernardini, L. Gallais, T. Fiorido, L. Patout, M. Bendahan, Ozone flexible sensors fabricated by photolithography and laser ablation processes based on ZnO nanoparticles, Sens. Actuators B 203 (2014) 602–611, https://doi.org/10.1016/j.snb.2014.07.010.

[100] Y.J. Onofre, A.C. Catto, S. Bernardini, T. Fiorido, K. Aguir, E. Longo, V. R. Mastelaro, L.F. da Silva, M.P.F. de Godoy, Highly selective ozone gas sensor based on nanocrystalline $Zn_{0.95}Co_{0.05}O$ thin film obtained via spray pyrolysis technique, Appl. Surf. Sci. 478 (2019) 347–354, https://doi.org/10.1016/j.apsusc.2019.01.197.

[101] G. Korotcenkov, B.K. Cho, L. Gulina, V. Tolstoy, Ozone sensors based on SnO_2 films modified by SnO_2-Au nanocomposites synthesized by the SILD method, Sens. Actuators B 138 (2) (2009) 512–517, https://doi.org/10.1016/j.snb.2009.01.058.

[102] Q. Simon, D. Barreca, A. Gasparotto, C. Maccato, E. Tondello, C. Sada, E. Comini, A. Devi, R.A. Fischer, Ag/ZnO nanomaterials as high performance sensors for flammable and toxic gases, Nanotechnology 23 (2) (2012) 025502, https://doi.org/10.1088/0957-4484/23/2/025502.

[103] A. Oprea, A. Gurlo, N. Bârsan, U. Weimar, Transport and gas sensing properties of In_2O_3 nanocrystalline thick films: a Hall effect based approach, Sens. Actuators B 139 (2) (2009) 322–328, https://doi.org/10.1016/j.snb.2009.03.002.

[104] B. Shanmugapriya, N. Moorthy, P. Dhamodharan, S. Suthakaran, T. Meganathan, A. Dinesh, L. Gnanasekaran, M. Ayyar, Fabrication of cubical-shaped particles/flakes/rods and flower-like morphology of In_2O_3 nanostructures: enhanced photocatalytic dye degradation and gas sensor applications, Inorg. Chem. Commun. 173 (2025) 113763, https://doi.org/10.1016/j.inoche.2024.113763.

[105] N. Sui, S. Cao, P. Zhang, T. Zhou, T. Zhang, The effect of different crystalline phases of In_2O_3 on the ozone sensing performance, J. Hazard. Mater. 418 (2021) 126290, https://doi.org/10.1016/j.jhazmat.2021.126290.

[106] B.S. de Lima, A.A. Komorizono, W.A.S. Silva, A.L. Ndiaye, J. Brunet, M.I. B. Bernardi, V.R. Mastelaro, Ozone detection in the ppt-level with rGO-ZnO based sensor, Sens. Actuators B 338 (2021) 129779, https://doi.org/10.1016/j.snb.2021.129779.

[107] X. Xu, M. Arab Pour Yazdi, J.B. Sanchez, A. Billard, F. Berger, N. Martin, Exploiting the dodecane and ozone sensing capabilities of nanostructured tungsten oxide films, Sens. Actuators B 266 (2018) 773–783, https://doi.org/10.1016/j.snb.2018.03.190.

[108] W.B. Wu, C.H. Hsu, X.X. Yue, W.Z. Zhang, J. Zhang, X.Y. Zhang, P. Gao, W.Y. Wu, D.S. Wuu, F.M. Lai, S.Y. Lien, Low temperature (002)-oriented zinc oxide films prepared using ozone-based spatial atomic layer deposition, Ceram. Int. 50 (15) (2024) 26770–26779, https://doi.org/10.1016/j.ceramint.2024.04.404.

[109] T. Dutta, T. Noushin, S. Tabassum, S.K. Mishra, Road map of semiconductor metal-oxide-based sensors: a review, Sensors 23 (15) (2023) 6849, https://doi.org/10.3390/s23156849.

[110] G. Korotcenkov, V. Nehasil, Ozone sensing by In_2O_3 films modified with Rh: dimension effect, Sensors 21 (5) (2021) 1886, https://doi.org/10.3390/s21051886.

[111] A.C. Catto, L.F. da Silva, C. Ribeiro, S. Bernardini, K. Aguir, E. Longo, V. R. Mastelaro, An easy method of preparing ozone gas sensors based on ZnO nanorods, RSC Adv. 5 (25) (2015) 19528–19533, https://doi.org/10.1039/c5ra00581g.

[112] G. Korotcenkov, I. Blinov, M. Ivanov, J.R. Stetter, Ozone sensors on the base of SnO_2 films deposited by spray pyrolysis, Sens. Actuators B 120 (2) (2007) 679–686, https://doi.org/10.1016/j.snb.2006.03.029.

[113] J. Huang, X. Wang, Y. Gong, Y. Liu, P. Zhou, X. Suo, D. Zeng, H. Li, Construction of WO_3 coatings with micro-nano hybrid structures by liquid precursor flame spray for enhanced sensing performances to sub-ppm ozone, Mater. Lett. 205 (2017) 106–109, https://doi.org/10.1016/j.matlet.2017.06.076.

[114] C.Y. Wang, S. Bagchi, M. Bitterling, R.W. Becker, K. Köhler, V. Cimalla, O. Ambacher, C. Chaumette, Photon stimulated ozone sensor based on indium oxide nanoparticles II: ozone monitoring in humidity and water environments, Sens. Actuators B 164 (1) (2012) 37–42, https://doi.org/10.1016/j.snb.2012.01.058.

[115] N. Sui, P. Zhang, S. Cao, T. Zhou, T. Zhang, Nanosheet-assembled In_2O_3 for sensitive and selective ozone detection at low temperature, J. Alloys Compd. 888 (2021) 161430, https://doi.org/10.1016/j.jallcom.2021.161430.

[116] M. Ivanovskaya, A. Gurlo, P. Bogdanov, Mechanism of O_3 and NO_2 detection and selectivity of In_2O_3 sensors, Sens. Actuators B 77 (1–2) (2001) 264–267, https://doi.org/10.1016/S0925-4005(01)00708-0.

[117] N. Sui, P. Zhang, T. Zhou, T. Zhang, Selective ppb-level ozone gas sensor based on hierarchical branch-like In_2O_3 nanostructure, Sens. Actuators B 336 (2021) 129612, https://doi.org/10.1016/j.snb.2021.129612.

[118] X. Xu, P. Zhao, D. Wang, P. Sun, L. You, Y. Sun, X. Liang, F. Liu, H. Chen, G. Lu, Preparation and gas sensing properties of hierarchical flower-like In2O3 microspheres, Sens. Actuators B 176 (2013) 405–412, https://doi.org/10.1016/j.snb.2012.10.091.

[119] G. Korotcenkov, A. Cerneavschi, V. Brinzari, A. Vasiliev, M. Ivanov, A. Cornet, J. Morante, A. Cabot, J. Arbiol, In_2O_3 films deposited by spray pyrolysis as a material for ozone gas sensors, Sens. Actuators B 99 (2–3) (2004) 297–303, https://doi.org/10.1016/j.snb.2003.01.001.

[120] F.S.S. Chien, C.R. Wang, Y.L. Chan, H.L. Lin, M.H. Chen, R.J. Wu, Fast-response ozone sensor with ZnO nanorods grown by chemical vapor deposition, Sens. Actuators B 144 (1) (2010) 120–125, https://doi.org/10.1016/j.snb.2009.10.043.

[121] D. Barreca, D. Bekermann, E. Comini, A. Devi, R.A. Fischer, A. Gasparotto, C. Maccato, C. Sada, G. Sberveglieri, E. Tondello, Urchin-like ZnO nanorod arrays for gas sensing applications, R. Soc. Chem. 12 (11) (2010) 3419, https://doi.org/10.1039/c0ce00139b.

[122] Y.T. Tsai, S.J. Chang, I.T. Tang, Y.J. Hsiao, L.W. Ji, High density novel porous ZnO nanosheets based on a microheater chip for ozone sensors, IEEE Sens. J. 18 (13) (2018) 5559–5565, https://doi.org/10.1109/Jsen.2018.2830508.

[123] Y.N. Colmenares, W. Correr, B.S. Lima, V.R. Mastelaro, The effect of morphology on the ozone-gas sensing properties of zinc oxide sputtered films, Thin Solid Films 703 (2020) 137975, https://doi.org/10.1016/j.tsf.2020.137975.

[124] W.A. dos Santos Silva, B.S. de Lima, M.I.B. Bernardi, V.R. Mastelaro, Enhancement of the ozone-sensing properties of ZnO through chemical-etched surface texturing, J. Nanopart. Res. 24 (5) (2022) 96, https://doi.org/10.1007/s11051-022-05479-3.

[125] A. Gaddari, F. Berger, M. Amjoud, J.B. Sanchez, M. Lahcini, B. Rhouta, D. Mezzane, C. Mavon, E. Beche, V. Flaud, A novel way for the synthesis of tin dioxide sol-gel derived thin films: application to O_3 detection at ambient temperature, Sens. Actuators B 176 (2013) 811–817, https://doi.org/10.1016/j.snb.2012.10.049.

[126] M. Belaqziz, M.b. Amjoud, A. Gaddari, B. Rhouta, D. Mezzane, Enhanced room temperature ozone response of SnO_2 thin film sensor, Superlattices Microstruct. 71 (2014) 185–189, https://doi.org/10.1016/j.spmi.2014.03.040.

[127] M. Bendahan, R. Boulmani, J. Seguin, K. Aguir, Characterization of ozone sensors based on WO_3 reactively sputtered films: influence of O_2 concentration in the sputtering gas, and working temperature, Sens. Actuators B 100 (3) (2004) 320–324, https://doi.org/10.1016/j.snb.2004.01.023.

[128] A.C. Catto, T. Fiorido, É.L.S. Souza, W. Avansi, J. Andres, K. Aguir, E. Longo, L. S. Cavalcante, L.F. da Silva, Improving the ozone gas-sensing properties of $CuWO_4$ nanoparticles, J. Alloys Compd. 748 (2018) 411–417, https://doi.org/10.1016/j.jallcom.2018.03.104.

[129] W.C. Huang, C. Chou, C.J. Yang, Y.M. Chen, W.J. Hsueh, S.Y. Liao, C.Y. Huang, Effect of ultraviolet light on Mn_3O_4 thin films that are grown using SILAR for room-temperature ozone gas sensors, J. Electrochem. Soc. 170 (8) (2023) 087516, https://doi.org/10.1149/1945-7111/acf244.

[130] J. Lv, C. Zhang, G. Qu, K. Pan, J. Qin, K. Wei, Y. Liang, Modification strategies for semiconductor metal oxide nanomaterials applied to chemiresistive NO_x gas sensors: a review, Talanta 273 (2024) 125853, https://doi.org/10.1016/j.talanta.2024.125853.

[131] J.F.d.S. Petruci, D.N. Barreto, M.A. Dias, E.P. Felix, A.A. Cardoso, Analytical methods applied for ozone gas detection: a review, TrAC Trends Anal. Chem. 149 (2022) 116552, https://doi.org/10.1016/j.trac.2022.116552.

[132] A. Dey, Semiconductor metal oxide gas sensors: a review, Mater. Sci. Eng. B Adv. 229 (2018) 206–217, https://doi.org/10.1016/j.mseb.2017.12.036.

[133] J.F. Tang, C.C. Fang, C.L. Hsu, Enhanced organic gas sensor based on Cerium- and Au-doped ZnO nanowires via low temperature one-pot synthesis, Appl. Surf. Sci. 613 (2023) 156094, https://doi.org/10.1016/j.apsusc.2022.156094.

[134] J. Li, H. Zhao, Y. Wang, Y. Zhou, Approaches for selectivity improvement of conductometric gas sensors: an overview, Sens. Diagn. 3 (3) (2024) 336–353, https://doi.org/10.1039/d3sd00226h.

[135] N. Sui, Z. Song, X. Xu, S. Cao, Y. Xu, T. Zhou, T. Zhang, Effect of heterogenous dopant and high temperature pulse excitation on ozone sensing behavior of In_2O_3 nanostructures and an image recognition method coupled to ozone sensing array, J. Hazard. Mater. 465 (2024) 133379, https://doi.org/10.1016/j.jhazmat.2023.133379.

[136] S. Bernardini, T. Fiorido, K. Aguir, O. Margeat, J. Ackermann, C. Videlot-Ackermann, UV-enhanced ozone sensing response of Al-doped zinc oxide nanocrystals at room temperature, Mater. Today 6 (2019) 310–313, https://doi.org/10.1016/j.matpr.2018.10.422.

[137] A. Paralikis, E. Gagaoudakis, V. Kampitakis, E. Aperathitis, G. Kiriakidis, V. Binas, Study on the ozone gas sensing properties of rf-sputtered Al-doped NiO films, Appl. Sci. 11 (7) (2021) 3104, https://doi.org/10.3390/app11073104.

[138] M. Zhao, W. Pan, Effect of lattice defects on thermal conductivity of Ti-doped, Y_2O_3-stabilized ZrO_2, Acta Mater. 61 (14) (2013) 5496–5503, https://doi.org/10.1016/j.actamat.2013.05.038.

[139] Z. Zhao, Z. Deng, R. Zhang, A. Klamchuen, Y. He, M. Horprathum, J. Chang, L. Mi, M. Li, S. Wang, X. Fang, G. Meng, Sensitive and selective ozone sensor based on $CuCo_2O_4$ synthesized by a facile solution combustion method, Sens. Actuators B 375 (2023) 132912, https://doi.org/10.1016/j.snb.2022.132912.

[140] Z. Cao, Z. Jiang, L. Cao, Y. Wang, C. Feng, C. Huang, Y. Li, Lattice expansion and oxygen vacancy of α-Fe_2O_3 during gas sensing, Talanta 221 (2021) 121616, https://doi.org/10.1016/j.talanta.2020.121616.

[141] E. Santos, A.C. Catto, A.F. Peterline, W. Avansi Jr, Transition metal (Nb and W) doped TiO_2 nanostructures: the role of metal doping in their photocatalytic activity and ozone gas-sensing performance, Appl. Surf. Sci. 579 (2022) 152146, https://doi.org/10.1016/j.apsusc.2021.152146.

[142] A.C. Catto, L.F. da Silva, M.I.B. Bernardi, S. Bernardini, K. Aguir, E. Longo, V. R. Mastelaro, Local structure and surface properties of $Co_xZn_{1\text{-}x}O$ thin films for ozone gas sensing, ACS Appl. Mater. Interfaces 8 (39) (2016) 26066–26072, https://doi.org/10.1021/acsami.6b08589.

[143] D.H. Sales, R.R. Leite, J.C.C.A. Diaz, A.A. Komorizono, M.I.B. Bernardi, V. R. Mastelaro, E. Longo, S.R. Teixeira, A.E. de Souza, Al-doped ZnO thin films via sputtering: influence of structural defects on ozone gas sensitivity, J. Mater. Res. 27 (suppl 2) (2024) e20240184, https://doi.org/10.1590/1980-5373.

[144] G. Korotcenkov, B.K. Cho, I. Boris, S.H. Han, Y. Lychkovsky, G. Karkotsky, Indium oxide ceramics doped by selenium for one-electrode gas sensors, Sens. Actuators B 174 (2012) 586–593, https://doi.org/10.1016/j.snb.2012.07.090.

[145] V. Moeini, A. Hossein Masoudi Gazi, Doped BC2NNTs with gallium: a new sensor to detect the presence of ozone gas in the gaseous environment, Comput. Theor. Chem. 1235 (2024) 114578, https://doi.org/10.1016/j.comptc.2024.114578.

[146] C.L. Zhu, H.L. Yu, Y. Zhang, T.S. Wang, Q.Y. Ouyang, L.H. Qi, Y.J. Chen, X.Y. Xue, Fe_2O_3/TiO_2 tube-like nanostructures: synthesis, structural transformation and the enhanced sensing properties, ACS Appl. Mater. Interfaces 4 (2) (2012) 665–671, https://doi.org/10.1021/am201689x.

[147] Z. Wang, L. Zhu, S.Y. Sun, J.N. Wang, W. Yan, One-dimensional nanomaterials in resistive gas sensor: from material design to application, Chemosensors 9 (8) (2021) 198, https://doi.org/10.3390/chemosensors9080198.

[148] K. Xu, K. Wu, J. Xu, M.P. Planche, S. Deng, H. Liao, C. Zhang, Metal oxide semiconductor-based heterojunctions synthesized by wet-chemical strategies for efficient volatile organic compounds detection, Coord. Chem. Rev. 538 (2025) 216735, https://doi.org/10.1016/j.ccr.2025.216735.

[149] H. Long, Y. Li, K. Chai, W. Zeng, Metal oxide semiconductor-based core-shell nanostructures for chemiresistive gas sensing: a review, Sens. Actuators B 417 (2024) 136183, https://doi.org/10.1016/j.snb.2024.136183.

[150] N. Sui, Y. Xu, P. Zhang, S. Cao, T. Zhou, T. Zhang, MIL-68 (In) and ZIF-8 assisted construction of n-n heterostructure for the effective sensing of trace-level ozone, Sens. Actuators B 380 (2023) 133312, https://doi.org/10.1016/j.snb.2023.133312.

[151] Z. Zhu, M.H. Chung, S.Q. Xu, R.J. Wu, Reduced graphene oxide-cuprous oxide composites for low concentration ozone detection, Sens. Actuators B 401 (2024) 135039, https://doi.org/10.1016/j.snb.2023.135039.

[152] K. Wetchakun, T. Samerjai, N. Tamaekong, C. Liewhiran, C. Siriwong, V. Kruefu, A. Wisitsoraat, A. Tuantranont, S. Phanichphant, Semiconducting metal oxides as sensors for environmentally hazardous gases, Sens. Actuators B 160 (1) (2011) 580–591, https://doi.org/10.1016/j.snb.2011.08.032.

[153] C.S. He, J.C. Ye, H.H. Zhang, X.R. Gong, X. Li, A review: strategies for enhancing the performance of SnO_2-based formaldehyde gas sensors, Microchem. J. 208 (2025) 112591, https://doi.org/10.1016/j.microc.2024.112591.

[154] S. Mohammad-Yousefi, S. Rahbarpour, H. Ghafoorifard, Describing the effect of Ag/Au modification on operating temperature and gas sensing properties of thick film SnO_2 gas sensors by gas diffusion theory, Mater. Chem. Phys. 227 (2019) 148–156, https://doi.org/10.1016/j.matchemphys.2019.02.010.

[155] H. Yang, K. Suematsu, K. Mitamura, R. Yanagawa, H. Saito, K. Watanabe, K. Shimanoe, Enhancement in gas sensing performance of MoO_3-loaded SnO_2 sensor via improving adsorption and partial oxidation, Sens. Actuators B 427 (2025) 137176, https://doi.org/10.1016/j.snb.2024.137176.

[156] Z.C. Tseng, Y.Y. Jiang, C.Y. Lin, J.Y. Do, T.H. Hsu, C.W. Shih, Y.Z. Chang, S. Y. Liao, C.Y. Huang, Highly stable flexible ozone gas sensors using Mn_3O_4 nanoparticles-decorated IGZO thin films through the SILAR method, Ceram. Int. 50 (16) (2024) 28584–28592, https://doi.org/10.1016/j.ceramint.2024.05.168.

[157] G. Korotcenkov, B.K. Cho, Ozone measuring: what can limit application of SnO_2-based conductometric gas sensors? Sens. Actuators B 161 (1) (2012) 28–44, https://doi.org/10.1016/j.snb.2011.12.003.

[158] J.Y. Liu, Z.X. Hu, Y.Z. Zhang, H.Y. Li, N.B. Gao, Z.L. Tian, L.C. Zhou, B.H. Zhang, J. Tang, J.B. Zhang, F. Yi, H. Liu, MoS_2 nanosheets sensitized with quantum dots for room-temperature gas sensors, Nano Micro Lett. 12 (1) (2020) 2–13, https://doi.org/10.1007/s40820-020-0394-6.

[159] U. Kumar, Y.N. Li, Z.Y. Deng, P.C. Chiang, B.C. Yadav, C.H. Wu, Nanoarchitectonics with lead sulfide quantum dots for room-temperature real-time ozone trace detection with different light exposure, J. Alloys Compd. 926 (2022) 166828, https://doi.org/10.1016/j.jallcom.2022.166828.

[160] K. Hu, F. Wang, Z. Shen, Y. Yan, H. Liu, Enhancement methods of hydrogen sensing for one-dimensional nanomaterials: a review, Int. J. Hydrog. Energy 46 (38) (2021) 20119–20138, https://doi.org/10.1016/j.ijhydene.2021.03.117.

[161] T. Thi Nguyet, L. Van Duy, N.C. Nam, D.Q. Dat, H. Nguyen, C.M. Hung, N. Van Duy, N.D. Hoa, Transition from p-type to n-type semiconductor in V_2O_5 nanowire-based gas sensors: synthesis and understanding of the sensing mechanism, Sens. Actuators B 424 (2025) 136841, https://doi.org/10.1016/j.snb.2024.136841.

[162] A.C. Catto, S. Bernardini, K. Aguir, E. Longo, L.F. da Silva, *In-situ* hydrothermal synthesis of oriented hematite nanorods for sub-ppm level detection of ozone gas, J. Alloys Compd. 947 (2023) 169444, https://doi.org/10.1016/j.jallcom.2023.169444.

[163] H. Bai, C. Feng, Y. Chen, Y. Du, Y. Feng, K. Liu, Y. Yan, J. Liu, B. Zhang, J. Wang, D. Chen, Y. Zheng, F. Guo, Room temperature gas sensor based on porous NiO nanoplates modified with rGO nanosheets and SnO_2 nanoparticles for accurate and rapid ppb-level NO_2 detection, Nano Mater. Sci. 006 (2025), https://doi.org/10.1016/j.nanoms.2024.12.006.

[164] J. Ding, M. Xie, Z. Li, Y. Wang, Fabrication of WO_3 nanosheets with hexagonal/orthorhombic homojunctions for highly sensitive ozone gas sensors at low temperature, J. Alloys Compd. 1010 (2025) 178228, https://doi.org/10.1016/j.jallcom.2024.178228.

[165] Y. Nagarjuna, Y.J. Hsiao, S.C. Wang, C.Y. Shao, Y.C. Huang, Nanoporous ZnO structure prepared by HiPIMS sputtering for enhanced ozone gas detection, Mater. Today Commun. 35 (2023) 106024, https://doi.org/10.1016/j.mtcomm.2023.106024.

[166] Q. Huang, Z. Deng, R. Zhang, A. Klamchuen, M. Horprathum, S. Wang, X. Fang, L. You, S. Huang, G. Meng, Highly sensitive and selective ppb-level ozone sensor based on porous CuO nanoparticles, Sens. Actuators B 406 (2024) 135434, https://doi.org/10.1016/j.snb.2024.135434.

[167] K.K. Pawar, A. Kumar, A. Mirzaei, M. Kumar, H.W. Kim, S.S. Kim, 2D nanomaterials for realization of flexible and wearable gas sensors: a review, Chemosphere 352 (2024) 141234, https://doi.org/10.1016/j.chemosphere.2024.141234.

[168] L. Koroglu, C. Aciksari, E. Ayas, E. Ozel, E. Suvaci, A comparative study of spark plasma and conventional sintering of undoped SnO_2 sputtering targets, Mater. Chem. Phys. 290 (2022) 126624, https://doi.org/10.1016/j.matchemphys.2022.126624.

[169] G. Manjunath, S. Pujari, D.R. Patil, S. Mandal, A scalable screen-printed high performance ZnO-UV and gas sensor: effect of solution combustion, Mater. Sci. Semicond. Process. 107 (2020) 104828, https://doi.org/10.1016/j.mssp.2019.104828.

[170] C. Martínez Pacheco, J.L. Cervantes López, A. del Rocío López-Guemez, A. S. López Rodríguez, P. Sifuentes Gallardo, J.C. Díaz Guillen, L.L. Díaz Flores, Preparation of ZnO thick films activated with UV-LED for efficient H_2S gas sensing, Coatings 14 (6) (2024) 693, https://doi.org/10.3390/coatings14060693.

[171] N.X. Thai, N. Van Duy, N. Van Toan, C.M. Hung, N. Van Hieu, N.D. Hoa, Effective monitoring and classification of hydrogen and ammonia gases with a bilayer Pt/SnO_2 thin film sensor, Int. J. Hydrog. Energy 45 (3) (2020) 2418–2428, https://doi.org/10.1016/j.ijhydene.2019.11.072.

[172] S. Pati, P. Banerji, S.B. Majumder, n- to p- type carrier reversal in nanocrystalline indium doped ZnO thin film gas sensors, Int. J. Hydrog. Energy 39 (27) (2014) 15134–15141, https://doi.org/10.1016/j.ijhydene.2014.07.075.

[173] X. Peng, J. Liu, Y. Tan, R. Mo, Y. Zhang, A CuO thin film type sensor via inkjet printing technology with high reproducibility for ppb-level formaldehyde detection, Sens. Actuators B 362 (2022) 131775, https://doi.org/10.1016/j.snb.2022.131775.

[174] G. Eranna, B.C. Joshi, D.P. Runthala, R.P. Gupta, Oxide materials for development of integrated gas sensors–a comprehensive review, Crit. Rev. Solid State Mater. Sci. 29 (3–4) (2010) 111–188, https://doi.org/10.1080/10408430490888977.

[175] G. Korotcenkov, V. Brinzari, B.K. Cho, In_2O_3- and SnO_2-based ozone sensors: design and characterization, Crit. Rev. Solid State Mater. Sci. 43 (2) (2017) 83–132, https://doi.org/10.1080/10408436.2017.1287661.

[176] E.Z. Tian, Q.P. Yu, Y.L. Gao, H. Wang, C. Wang, Y.P. Zhang, B.H. Li, M.F. Zhu, J. H. Mo, G.Y. Xu, J. Li, Ultralow resistance two-stage electrostatically assisted air filtration by polydopamine coated PET coarse filter, Small 17 (33) (2021) 2102051, https://doi.org/10.1002/smll.202102051.

[177] S.V. Ryabtsev, N.Y. Obvintseva, D.A.A. Ghareeb, A.A.K. Al-Habeeb, A. V. Shaposhnik, S.Y. Turishchev, E.P. Domashevskaya, Thin-film oxide materials for ozone detection in thermal modulation mode, Inorg. Mater. 59 (5) (2023) 487–493, https://doi.org/10.1134/S0020168523050151.

[178] C.Y. Huang, X.R. He, C.T. Huang, Realization of a self-powered InGaZnO MSM ozone sensor via a surface state modulated photovoltaic effect, ACS Appl. Electron. Mater. 4 (11) (2022) 5437–5445, https://doi.org/10.1021/acsaelm.2c01099.

[179] Z.Y. Yuan, F. Yang, F.L. Meng, K.Y. Zuo, J. Li, Research of low-power MEMS-based micro hotplates gas sensor: a review, IEEE Sens. 21 (17) (2021) 18368–18380, https://doi.org/10.1109/Jsen.2021.3088440.

[180] C.H. Zhao, H.M. Gong, G.Q. Niu, F. Wang, MEMS gas sensors-from nanomaterials to microelectrodes, in: Proceedings of the IEEE MEMS, 2020, pp. 194–199, https://doi.org/10.1109/mems46641.2020.9056235.

[181] D.B. Guan, F. Yang, Q. Liu, K. Yu, J. Sun, A novel prototype of low power consumption MEMS sensors for hydrogen detection, in: Proceedings of the IEEE MEMS, 2016 7808659, https://doi.org/10.1109/ICSENS.2016.7808659.

[182] G. Niu, F. Wang, A review of MEMS-based metal oxide semiconductors gas sensor in Mainland China, J. Micromech. Microeng. 32 (5) (2022) 054003, https://doi.org/10.1088/1361-6439/ac5b98.

[183] Y. Nagarjuna, Y.J. Hsiao, W.T. Hsiao, Z.X. Li, M. Lin, Enhanced ozone gas detection with Sb doped ZnO nanorods synthesized on MEMS microheater, Sens. Actuators Rep. 7 (2024) 100191, https://doi.org/10.1016/j.snr.2024.100191.

[184] G.Q. Niu, C.H. Zhao, H.M. Gong, Y.S. Hu, Y.L. Zhang, Z.T. Zhou, T.H. Tao, F. Wang, A micro-hotplate for MEMS-based H_2S sensor, in: Proceedings of the IEEE MEMS, 2019, pp. 1153–1156, https://doi.org/10.1109/transducers.2019.8808648.

[185] G.Q. Niu, H.M. Gong, C.H. Zhao, F. Wang, H_2S sensor based on mems hotplate and on-chip growth of CuO-SnO_2 nanosheets for high response, fast recovery and low power consumption, in: Proceedings of the IEEE MEMS, 2020, pp. 799–802, https://doi.org/10.1109/mems46641.2020.9056397.

[186] N.G. Iyer, S. Suganthi, M. Arulmozhi, P. Sivakumar, S. Jeny Sophia, Design and evaluation of micro-heater geometries for MEMS-based ozone gas sensor through a theoretical modeling, Mater. Today 66 (2022) 2012–2016, https://doi.org/10.1016/j.matpr.2022.05.446.

[187] M.Y. Liu, C.Z. Hang, X.F. Zhao, L.Y. Zhu, R.G. Ma, J.C. Wang, H.L. Lu, D. W. Zhang, Advance on flexible pressure sensors based on metal and carbonaceous nanomaterial, Nano Energy 87 (2021) 106181, https://doi.org/10.1016/j.nanoen.2021.106181.

[188] J.Y. Yong, W.G. Hong, N.J. Choi, H.K. Byung, Y. Jun, H.K. Lee, Ultrasensitive and highly selective graphene-based single yarn for use in wearable gas sensor, Sci. Rep. 5 (1) (2015) 10904, https://doi.org/10.1038/srep10904.

[189] G. Yang, C. Lee, J. Kim, F. Ren, S.J. Pearton, Flexible graphene-based chemical sensors on paper substrates, Phys. Chem. Chem. Phys. 15 (6) (2013) 1798–1801, https://doi.org/10.1039/c2cp43717a.

[190] N. Tang, C. Zhou, L.H. Xu, Y. Jiang, H.M. Qu, X.X. Duan, A fully integrated wireless flexible ammonia sensor fabricated by soft nano-lithography, ACS Sens. 4 (3) (2019) 726–732, https://doi.org/10.1021/acssensors.8b01690.

[191] P. Goswami, G. Gupta, Recent progress of flexible NO_2 and NH_3 gas sensors based on transition metal dichalcogenides for room temperature sensing, Mater. Today Chem. 23 (2022) 100726, https://doi.org/10.1016/j.mtchem.2021.100726.

[192] S.D. Lawaniya, S. Kumar, Y. Yu, H.G. Rubahn, Y.K. Mishra, K. Awasthi, Functional nanomaterials in flexible gas sensors: recent progress and future prospects, Mater. Today Chem. 29 (2023) 101428, https://doi.org/10.1016/j.mtchem.2023.101428.

[193] C.Y. Lee, G.W. Wu, W.J. Hsieh, Fabrication of micro sensors on a flexible substrate, Sens. Actuators A 147 (1) (2008) 173–176, https://doi.org/10.1016/j.sna.2008.05.004.